

Robust covariance estimation of galaxy-galaxy weak lensing: validation and limitation of jackknife covariance

Masato Shirasaki^{1*}, Masahiro Takada², Hironao Miyatake^{3,2}, Ryuichi Takahashi⁴, Takashi Hamana¹, Takahiro Nishimichi,^{2,5} and Ryoma Murata^{2,6}

¹*National Astronomical Observatory of Japan, Mitaka, Tokyo 181-8588, Japan*

²*Kavli Institute for the Physics and Mathematics of the Universe (WPI), The University of Tokyo Institutes for Advanced Study (UTIAS), The University of Tokyo, 5-1-5 Kashiwanoha, Kashiwa-shi, Chiba, 277-8583, Japan*

³*Jet Propulsion Laboratory, California Institute of Technology, Pasadena, CA 91109, USA*

⁴*Faculty of Science and Technology, Hirosaki University, 3 Bunkyo-cho, Hirosaki, Aomori, 036-8561, Japan*

⁵*CREST, JST, 4-1-8 Honcho, Kawaguchi, Saitama, 332-0012, Japan*

⁶*Department of Physics, School of Science, The University of Tokyo, 7-3-1 Hongo, Bunkyo, Tokyo 113-0033, Japan*

ABSTRACT

We develop a method to simulate galaxy-galaxy weak lensing by utilizing all-sky, light-cone simulations and their inherent halo catalogs. Using the mock catalog to study the error covariance matrix of galaxy-galaxy weak lensing, we compare the full covariance with the “jackknife” (JK) covariance, the method often used in the literature that estimates the covariance from the resamples of the data itself. We show that there exists the variation of JK covariance over realizations of mock lensing measurements, while the average JK covariance over mocks can give a reasonably accurate estimation of the true covariance up to separations comparable with the size of JK subregion. The scatter in JK covariances is found to be $\sim 10\%$ after we subtract the lensing measurement around random points. However, the JK method tends to underestimate the covariance at the larger separations, more increasingly for a survey with a higher number density of source galaxies. We apply our method to the Sloan Digital Sky Survey (SDSS) data, and show that the 48 mock SDSS catalogs nicely reproduce the signals and the JK covariance measured from the real data. We then argue that the use of the accurate covariance, compared to the JK covariance, allows us to use the lensing signals at large scales beyond a size of the JK subregion, which contains cleaner cosmological information in the linear regime.

Key words: gravitational lensing: weak — cosmology: observations — method: numerical

1 INTRODUCTION

Cross-correlation of large-scale structure (LSS) tracers, galaxies or clusters, with shapes of background galaxies, referred as to galaxy-galaxy weak lensing or stacked lensing, offers a unique means of measuring the average total matter distribution around the foreground objects at lens redshift (Brainerd, Blandford & Smail 1996; Hudson et al. 1998; Fischer et al. 2000; Guzik & Seljak 2002; Hoekstra, Yee & Gladders 2004; Mandelbaum et al. 2006; Johnston et al. 2007; Okabe et al. 2013; Gillis et al. 2013; Velander et al. 2014). In particular, by combining the weak lensing and auto-clustering correlation of the same foreground tracers, one can recover the underlying matter clustering and then constrain cosmology by breaking the degeneracy with galaxy bias uncertainty (e.g., Seljak et al. 2005; Cacciato et al. 2009; Mandelbaum et al. 2013; More et al. 2015; Kwan et al. 2016). Combining different probes of LSS and cosmic microwave background (CMB) will become a standard strategy aimed at achieving the full potential of ongoing and upcoming wide-area galaxy surveys for addressing the fundamental physics with the cosmological observables (e.g., Oguri & Takada 2011; Schaun et al. 2016). The surveys include the Baryon Oscillation Spectroscopic Survey (BOSS), the Dark Energy Survey (DES)¹, the Kilo-Degree Survey (KiDS)², the Subaru Hyper Suprime-Cam (HSC)

* E-mail: masato.shirasaki@nao.ac.jp

¹ <http://hsc.mtk.nao.ac.jp/ssp/>

² <http://kids.strw.leidenuniv.nl>

survey³, the Dark Energy Spectroscopic Instrument (DESI)⁴, and the Subaru Prime Focus Spectrograph (PFS) survey (Takada et al. 2014) in coming 5 years, and ultimately the Large Synoptic Survey Telescope (LSST)⁵, Euclid⁶ and WFIRST⁷ within a coming 10 year time scale.

In order to properly extract cosmological information from a given survey, it is important to understand the statistical properties of LSS probes that arise from the properties of the underlying matter distribution. The statistical precision of galaxy-galaxy weak lensing measurements is determined by the covariance matrix that itself contains two contributions: the measurement noise and sample variance caused by an incomplete sampling of the fluctuations due to a finite size of a survey volume. An accurate estimation of the covariance is becoming a challenging issue for upcoming wide-area galaxy surveys (Hartlap, Simon & Schneider 2007; Dodelson & Schneider 2013; Taylor, Joachimi & Kitching 2013), especially if the dimension of data vector is large, e.g. when combining different LSS probes.

Even though the initial density field is nearly Gaussian, the sample variance of LSS probes gets substantial non-Gaussian contributions from the nonlinear evolution of large-scale structure (e.g., Scoccimarro, Zaldarriaga & Hui 1999; Cooray & Hu 2001). Since the different Fourier modes are no longer independent but rather are correlated with each other in the weakly or deeply nonlinear regime, it is important to accurately model the non-Gaussian contribution to the sample variance. For this, it is now recognized that the super-sample covariance (SSC), which arises from mode-couplings of sub-survey (observable) modes with super-survey (unobservable) modes comparable with or greater than the size of a survey volume, is the largest non-Gaussian contribution to the sample variance for the cluster counts, the matter power spectrum and the cosmic shear statistics (Hu & Kravtsov 2003; Hamilton, Rimes & Scoccimarro 2006; Takada & Bridle 2007; Takada & Jain 2009; Sato et al. 2009, 2011; Takahashi et al. 2009; Kayo, Takada & Jain 2013; Kayo & Takada 2013; Takada & Hu 2013; Takada & Spergel 2014; Schaan, Takada & Spergel 2014; Takahashi et al. 2014; Li, Hu & Takada 2014b; Shirasaki, Hamana & Yoshida 2015; Krause & Eifler 2016; Mohammed, Seljak & Vlah 2016). In particular Takada & Hu (2013) developed a unified approach to describing the SSC effect in terms of the response of a given observable to a background mode modeling the super-survey mode (also see Li, Hu & Takada 2014a,b). Several cosmic shear measurements have taken into account the SSC contribution in the cosmological analysis (Becker et al. 2015; Harnois-Déraps et al. 2016; Hildebrandt et al. 2016).

However, the covariance matrix of galaxy-galaxy weak lensing has not been fully studied. A commonly-used approach to estimating the covariance is the jackknife method, which is a well-known method in the fields of statistics or data analysis (Efron 1982) (also see Bothun et al. 1983, for the pioneer cosmological applications). The JK method gives an internal estimator of the errors, i.e. estimating the covariance from the resamples of subdivided copies of the data itself (e.g., Mandelbaum et al. 2013; Cacciato, van Uitert & Hoekstra 2014; Coupon et al. 2015; Miyatake et al. 2016b; Clampitt et al. 2016, for the use of JK covariance for the galaxy-galaxy weak lensing). The advantage of the JK method is that it can account for various observational effects inherent in the data, such as inhomogeneities in the depth and measurements across the area. However, the drawback is that the JK covariance is generally noisy because it is estimated from one particular realization of the fluctuations, i.e. data itself. For the same reason, the JK covariance can be unstable or even singular especially if the dimension of data vector is comparable with the number of JK resamples, which could often happen if dividing the data into different bins of the physical quantities or combining different probes. Furthermore, Singh et al. (2016) recently showed that the use of the random catalog of lensing galaxies (or clusters) is important for the covariance estimation of galaxy-galaxy lensing, differently from the cosmic shear covariance. What does the JK method really estimate? What are the limitations? These questions have not been fully addressed yet (also see Norberg et al. 2009, for a study based on the similar motivation for the clustering correlation function). In particular it is not clear whether the JK method can capture the SSC contribution in the galaxy-galaxy weak lensing measurements.

Hence the purpose of this paper is to study the covariance matrix of galaxy-galaxy weak lensing. To do this, we develop a method to construct a mock catalog of the galaxy-galaxy weak lensing measurements by fully utilizing a set of full-sky, light-cone simulations containing the lensing fields in multiple source planes as well as dark matter and halo distributions in multiple lens planes (Shirasaki, Hamana & Yoshida 2015) (also see Takahashi et al. in preparation). In order to properly simulate properties of source galaxies, we populate a “real” catalog of source galaxies into the light-cone simulation realization (also see Shirasaki & Yoshida 2014). In this way we can take into account the observed characteristics of source galaxies (their angular distributions, redshifts, intrinsic ellipticities, and the survey geometry). By identifying halos that are considered to host galaxies and clusters as for foreground tracers, based on a prescription such as the halo occupation distribution and the halo mass-cluster observable scaling relation, we can make hypothetical galaxy-galaxy weak lensing measurements from the mock catalog. With the help of such mock catalogs, we will study the importance of the SSC contribution to the sample variance in the galaxy-galaxy weak lensing as well as the limitations of the JK method. We then apply the developed method to the Sloan Digital Sky Survey (SDSS) data: the catalog of source galaxies (Mandelbaum et al. 2013) and the lens samples of redMaPPer clusters (Rykoff et al. 2014) and the luminous red galaxies (Eisenstein et al. 2001). We will also discuss how the use of accurate covariance could improve cosmological constraints, compared to the JK method.

The paper is organized as follows. Section 2 summarizes basics of galaxy-galaxy weak lensing, the estimator of the signal, and the different covariance estimators. Section 3 describes the details of N -body simulations, halo catalogs and ray-tracing simulations used in this paper, and describes the details of our method for generating mock catalogs of galaxy-galaxy weak lensing. Section 4 presents the main

³ <http://hsc.mtk.nao.ac.jp/ssp/>

⁴ <http://desi.lbl.gov>

⁵ <https://www.lsst.org>

⁶ <http://sci.esa.int/euclid/>

⁷ <http://wfirst.gsfc.nasa.gov>

results including detailed comparison of the different covariance estimators as well as the application to the real SDSS data. We discuss the results in Section 5.

2 GALAXY-GALAXY WEAK LENSING

2.1 Basics

Cross-correlating positions of large-scale structure tracers, galaxies or galaxy clusters, with shapes of background galaxies, known as galaxy-galaxy weak lensing or stacked cluster lensing, measures the average mass distribution around the foreground objects:

$$\Sigma(R) = \bar{\rho}_{m0} \int d\chi \left[1 + \xi_{lm} \left(\sqrt{\chi^2 + R^2} \right) \right], \quad (1)$$

where $\bar{\rho}_{m0}$ is the mean matter density of the universe today, χ is the comoving radial separation, and R is the projected separation. $\xi_{lm}(r)$ is the three-dimensional cross-correlation of matter and lensing objects:

$$\xi_{lm}(r) = \langle \delta_l(\mathbf{x}) \delta_m(\mathbf{x} + \mathbf{r}) \rangle, \quad (2)$$

where $\delta_l(\mathbf{x})$ is the number density fluctuation field of lensing objects and $\delta_m(\mathbf{x})$ is the mass density fluctuation field. The surface mass density profile is related to the observable quantity of weak lensing, the tangential shear distortion γ_+ of the shapes of background galaxies, via

$$\Delta\Sigma(R) = \Sigma_{cr}\gamma_+(R) = \bar{\Sigma}(R) - \Sigma(R), \quad (3)$$

where $\Sigma_{cr}(z_l, z_s)$ is the lensing efficiency function, defined for a system of lens objects and sources at redshifts z_l and z_s , respectively, for a flat universe as

$$\Sigma_{cr}(z_l, z_s)^{-1} = 4\pi G(1 + z_l)\chi(z_l) \left[1 - \frac{\chi(z_l)}{\chi(z_s)} \right], \quad (4)$$

where $\chi(z)$ is the comoving radial distance to redshift z . The subscripts “l” or “s” stand for lens or source respectively. We will often call $\Delta\Sigma$ the excess surface mass density profile. In practice, we need to properly take into account the redshift distributions of lensing objects and source galaxies in the galaxy-galaxy weak lensing measurements.

Taking into account the redshift width of lensing objects and the connection of lensing objects with the underlying halo distribution, the lensing profile $\Delta\Sigma(R)$ can also be expressed as

$$\Delta\Sigma(R) = \frac{\bar{\rho}_{m0}}{\bar{N}_l} \int d\chi f_l(\chi; z_l) \int dM \frac{dn}{dM} S_l(M; \chi) \int \frac{kdk}{2\pi} P_{hm}(k; M, \chi) J_2(kR), \quad (5)$$

where

$$\bar{N}_l = \int d\chi f_l(\chi; z_l) \int dM \frac{dn}{dM} S_l(M; \chi). \quad (6)$$

Here \bar{N}_l is the average projected number density of lensing objects in units of $[\text{Mpc}^{-2}]$, $f_l(\chi; z_l)$ is the radial selection function for lensing objects around z_l , dn/dM is the halo mass function, $S_l(M)$ is the selection function of halos that describes how to populate lensing objects into halos of mass M and at redshift $z = z(\chi)$ in an average sense (e.g. the halo occupation distribution), $P_{hm}(k; M, \chi)$ is the cross-power spectrum between distributions of matter and halos with M and z , and $J_2(x)$ is the second-order Bessel function. The above equation implicitly assumes that each lensing object is at the center of its host halo. If off-centered lensing objects are included in the analysis, the equation needs to be modified, according to the method in Oguri & Takada (2011) (also see Hikage, Takada & Spergel 2012; Hikage et al. 2013; More et al. 2015).

2.2 Estimator of galaxy-galaxy weak lensing

In an actual observation, the galaxy-galaxy weak lensing has to be estimated from the observed ellipticities of source galaxies. In this paper, we employ the estimator of $\Delta\Sigma$ in Mandelbaum et al. (2013);

$$\widehat{\Delta\Sigma}(R) \equiv \frac{1}{2\mathcal{R}} \left[\frac{1}{\bar{N}_{ls}} \sum_{l,s} \Sigma_{cr}(z_l, z_s) w_{ls} \epsilon_+(\boldsymbol{\theta}_s) \Big|_{R=\chi_l \Delta\theta} - \frac{1}{\bar{N}_{rs}} \sum_{r,s} \Sigma_{cr}(z_r, z_s) w_{rs} \epsilon_+(\boldsymbol{\theta}_s) \Big|_{R=\chi_r \Delta\theta} \right], \quad (7)$$

where the subscript “r” denotes the random catalog of lensing objects, the projected (comoving) radius R are estimated from the observed angular separation for lens- or random-source pair, $\Delta\theta$, e.g., via $R = \chi_l \Delta\theta$, ϵ_+ represents the tangential component of observed ellipticity of source with respect to the center of lensing object or random point, and w_{ls} or w_{rs} is the weight. The summation runs over all the pairs of sources and lenses (or randoms) separated by the projected radius R to within a given bin width. \mathcal{R} is the responsivity that is needed for conversion of ellipticity to lensing shear γ_+ , due to the definition of ellipticity used in this paper (Bernstein & Jarvis 2002). Note that the random catalog is built so as to follow the survey geometry (boundary) and the survey depth as well as to resemble properties of lensing objects such as the redshift distribution and the halo mass distribution. The above estimator is defined in analogy with Landy & Szalay

(1993). The stacked lensing around random points is generally non-zero at large radii due to a violation of periodic boundary conditions in a general survey geometry. The non-lensing (B -mode) signal is also non-zero at the large radii for the same reason. The subtraction of the stacked lensing around random points corrects for these effects. Furthermore, as pointed out in Singh et al. (2016), the use of the random catalogs is important for the covariance estimation of galaxy-galaxy weak lensing.

Again following Mandelbaum et al. (2013), we employ the weight that is motivated by the inverse variance weighting, assuming that the measurement error is dominated by the intrinsic ellipticity on individual galaxy basis:

$$w_{\text{ls}} = \frac{1}{\Sigma_{\text{cr}}(z_1, z_s)^2 (\sigma_\epsilon^2 + \sigma_{\text{SN}}^2)}, \quad (8)$$

where σ_{SN} is the rms intrinsic ellipticity and σ_ϵ is the measurement error of galaxy ellipticity. The factor of Σ_{cr}^{-2} accounts for downweighting pairs that are close in redshift because the lensing efficiency is suboptimal. In reality, we might need to make further corrections of other residual systematic errors at each radial bin e.g., a multiplicative bias in shape measurements and an inclusion of unlensed galaxies into the source galaxy sample (see Mandelbaum et al. 2005, for details). The weight for the random points, w_{rs} , is defined in the similar manner to the above equation, since each random point has assigned ellipticity, measurement error and redshift that mimic the distributions of lensing galaxies or clusters.

Let us give an intuitive expression of the galaxy-galaxy lensing that might be useful for the following discussion. Suppose that the observed ellipticity of a source galaxy is given as a sum of the intrinsic shape and the lensing distortion effect due to the intervening matter distribution in the weak lensing regime:

$$\epsilon_+ \simeq \epsilon_+^{\text{int}} + \gamma_+(\boldsymbol{\theta}_s) \quad (9)$$

The lensing field γ_+ is equivalent to the lensing convergence field and is expressed in terms of the mass density fluctuation field as

$$\begin{aligned} \gamma_+(\boldsymbol{\theta}_s) \leftrightarrow \kappa(\boldsymbol{\theta}_s) &= \bar{\rho}_{\text{m}0} \int_0^{\chi_s} d\chi \Sigma_{\text{cr}}(\chi, \chi_s)^{-1} \delta_{\text{m}}(\chi, \chi\boldsymbol{\theta}_s) \\ &\simeq \bar{\rho}_{\text{m}0} \Sigma_{\text{cr}}(z_1, z_s)^{-1} \int_{\text{around } z_1} d\chi \delta_{\text{m}}(\chi, \chi\boldsymbol{\theta}_s) + \bar{\rho}_{\text{m}0} \int_{z \neq z_1} d\chi \Sigma_{\text{cr}}(\chi, \chi_s)^{-1} \delta_{\text{m}}(\chi, \chi\boldsymbol{\theta}_s). \end{aligned} \quad (10)$$

In the last line on the r.h.s. we intended to explicitly show that the lensing effect on a source galaxy in the direction $\boldsymbol{\theta}_s$ and at redshift z_s arises from the mass distribution in the lens planes around redshift z_1 as well as all the mass distribution along the line of sight. This equation shows that, by cross-correlating the shapes of background galaxies with positions of lensing objects in a particular range of lens redshift, we can probe the average mass distribution in the lens planes (the first term on the r.h.s.), while the matter distribution at different redshifts causes statistical errors (the 2nd term).

2.3 Covariance matrix

The covariance matrix characterizes statistical errors in measurements of the stacked lensing profile. The statistical errors arise from the shape noise of source galaxies, the shot noise arising due to a finite number of lens-source pairs, and the sample variance of large-scale structure at lens redshift and along the line of sight.

As discussed in Takada & Hu (2013), the covariance matrix is generally expressed by a sum of the three distinct contributions, the Gaussian covariance, the non-Gaussian (NG) covariance and the super-sample covariance (SSC), respectively:

$$\begin{aligned} \mathbf{C}_{ij} &\equiv \left\langle \widehat{\Delta\Sigma}(R_i) \widehat{\Delta\Sigma}(R_j) \right\rangle - \left\langle \widehat{\Delta\Sigma}(R_i) \right\rangle \left\langle \widehat{\Delta\Sigma}(R_j) \right\rangle \\ &= \mathbf{C}_{ij}^{\text{Gauss}} + \mathbf{C}_{ij}^{\text{NG}0} + \mathbf{C}_{ij}^{\text{SSC}}. \end{aligned} \quad (11)$$

Exactly speaking, the SSC contribution is a part of the non-Gaussian covariance, but we separated the SSC because it arises from super-survey modes, the mass density fluctuation field whose length scales are comparable with or greater than a size of the survey region. With this decomposition, we impose that the non-Gaussian term $\mathbf{C}^{\text{NG}0}$ arises from the trispectrum of sub-survey modes. The Gaussian and non-Gaussian terms, \mathbf{C}^{G} and $\mathbf{C}^{\text{NG}0}$, scale with survey area (Ω_s) as $\mathbf{C}^{\text{Gauss}}$, $\mathbf{C}^{\text{NG}0} \propto 1/\Omega_s$. The SSC amplitude scales with the variance of the coherent density mode in the survey window at each lens redshift, $\sigma_{\text{b},z_1}^2 \equiv \langle \delta_{\text{b},z_1}^2 \rangle$, where $\delta_{\text{b},z_1} = \int d^3\mathbf{x} \delta_{\text{m}}(\mathbf{x}) W(\mathbf{x}; z_1)$ and $W(\mathbf{x}; z_1)$ is the survey window around the lens slice at z_1 . For a fixed area, the amplitude also depends on the survey geometry (Takada & Hu 2013; Takahashi et al. 2014). Thus the SSC causes a complication in the covariance estimation: since the super-survey modes are not a direct observable from a given survey, one has to model the contribution theoretically, either based on the analytic method or the mock catalogs based on simulations properly including the super-survey modes. This paper employs the latter approach.

The goal of this paper is to develop a method of accurately estimating the covariance matrix for a given survey as well as to develop a physical understanding of how each term in equation (11) contributes the covariance matrix for ongoing and existing surveys such as the SDSS dataset. In the literature, several methods for the covariance estimation have been considered. For example, one way is the jackknife method, which is an approximated, practical method, but enables us to estimate the covariance matrix from the real data itself. Another way is the method using mock catalogs of the universe (lensing objects and weak lensing fields). In the following we define the different covariance estimators considered in this paper, and then discuss pros and cons of each method.

2.3.1 “Full” covariance based on the mock catalogs

This should be a most accurate method if we have accurate mock catalogs of the lensing observables (source galaxies and lensing galaxies or clusters) for a given survey as well as a sufficient number of the realizations for an assumed cosmological model. Building such mock catalogs requires adequately-designed numerical simulations. However, this is tricky and involves conflicting requirements. If a survey area is wide, one has to include very large-scale modes in the light cone, which requires a very large-box simulation. On the other hand, simulating lens objects, either galaxies or clusters, requires an adequately high-resolution simulation in order to resolve halos and/or subhalos and then relate the halos/subhalos to lensing galaxies or clusters. In addition, an accurate estimation of the covariance matrix requires a sufficiently large number of independent realizations of the mock catalogs, further ideally as a function of cosmological models. These requirements are not readily met by currently-available computational resources.

Once the adequately accurate mock catalogs and their realizations are available, we can estimate the covariance matrix using realizations of the mock catalogs:

$$\mathbf{C}^{\text{full}}(R_i, R_j) = \frac{1}{N_r - 1} \sum_{a=1}^{N_r} \left[\widehat{\Delta\Sigma}_{(a)}(R_i) - \overline{\Delta\Sigma}(R_i) \right] \left[\widehat{\Delta\Sigma}_{(a)}(R_j) - \overline{\Delta\Sigma}(R_j) \right] \quad (12)$$

where $\widehat{\Delta\Sigma}_{(a)}(R_i)$ is the lensing profile at the radial bin R_i estimated from the a -th realization of the mock catalog, and N_r is the number of the realizations. $\overline{\Delta\Sigma}$ is the average of the lensing profiles over all the realizations:

$$\overline{\Delta\Sigma}(R_i) = \frac{1}{N_r} \sum_{a=1}^{N_r} \Delta\Sigma_{(a)}(R_i). \quad (13)$$

We hereafter call the covariance estimator (equation 12) “full covariance”. An advantage of this method is we can properly take into account the SSC contribution, if the mock catalogs include the super-survey modes for a given survey geometry. A disadvantage is that the accuracy of the covariance estimation depends on the accuracy of mock catalogs, which requires adequate computational resources to perform suitable N -body simulations as well as ray-tracing simulations.

Cosmic sample variances in measurements of the stacked lensing profile $\widehat{\Delta\Sigma}$ arise from statistical properties of large-scale structure in the light cone from an observer to source galaxies. The difference from the cosmic shear statistics is that, in addition to the matter distribution in the light cone, we need to model sample variance arising from the distribution of lensing objects (halos we will consider) and the cross-correlation with their surrounding matter distribution at particular lens redshifts. In order to properly model the statistical properties of stacked lensing, we will use a suite of high-resolution N -body simulations as well as ray-tracing simulations that are computed by tracing light rays through the simulated matter distribution in the light cone, as we describe below.

2.3.2 Jackknife method

The jackknife (JK) method is one of the techniques most conventionally used for estimating the covariance matrix in the literature. The JK method allows one to estimate the covariance matrix of stacked lensing from the data itself. The implementation is as follows. (1) Divide the survey region into different N_{sub} subregions, where each subregion is defined so as to have an equal (or roughly equal) area. (2) Estimate the stacked lensing profile from the survey region, but excluding each of the N_{sub} subregions. We call this measurement excluding the α -th subregion “the α -th JK resample”. (3) Repeat the (2) measurements for all the N_{sub} subregions, and then construct the N_{sub} JK resamples. By construction, each JK resample consists of $(N_{\text{sub}} - 1)$ subregions that has a smaller area than that of the original dataset by a factor of $(N_{\text{sub}} - 1)/N_{\text{sub}}$. (4) The covariance matrix is estimated from the N_{sub} JK resamples as

$$\mathbf{C}^{\text{JK}}(R_i, R_j) = \frac{N_{\text{sub}} - 1}{N_{\text{sub}}} \sum_{\alpha=1}^{N_{\text{sub}}} \left[\widehat{\Delta\Sigma}_{(\alpha)}(R_i) - \overline{\Delta\Sigma}(R_i) \right] \left[\widehat{\Delta\Sigma}_{(\alpha)}(R_j) - \overline{\Delta\Sigma}(R_j) \right], \quad (14)$$

where $\widehat{\Delta\Sigma}_{(\alpha)}(R_j)$ is the lensing measurement for the α -th JK resample, and

$$\overline{\Delta\Sigma}(R_i) \equiv \frac{1}{N_{\text{sub}}} \sum_{\alpha=1}^{N_{\text{sub}}} \widehat{\Delta\Sigma}_{(\alpha)}(R_i) \quad (15)$$

The concept of the JK method is the different JK resamples give different realizations of the measurements, which then enable one to estimate the covariance. It is known that the JK method gives an unbiased estimator of the underlying true covariance if the mass and galaxy distributions in large-scale structure obey a random Gaussian or Poisson distribution. However, the fields are non-Gaussian, and all the different modes are correlated with each other. In particular, it has not been fully addressed whether the JK method captures the SSC contribution for a given survey region. Addressing this question is one of our main scopes.

The advantage of the JK method is that, since the JK covariance is estimated from the actual dataset itself, it automatically incorporate observational effects on the covariance estimation, e.g., possible inhomogeneities in the depth of data and selection function of lensing galaxies and/or source galaxies. However, there are several caveats that must be kept in mind. First, the accuracy of JK covariance estimation depends on the number of JK subregions. If an insufficient number of JK subregions are taken, the covariance estimation becomes noisy because the insufficient JK resamples cannot well capture the underlying variations in the stacked lensing. Second, the size of JK subregion

sets a maximum separation scale of the stacked lensing profile used for the cosmological analysis, because the JK resamples would by construction display less variations in the stacked lensing profile at larger separations than the JK subregion size. Since the stacked lensing profile at large separations contains a cleaner cosmological information in the weakly nonlinear or linear regime, we want to have an access to such large separations. Hence there is a trade-off in the JK subdivisions of dataset: the number of JK subregions vs. the maximum separation scale. If we want to use the large separation, we need to take a relatively large-area JK subregion, yielding a relatively small number of JK resamples, and then the covariance estimation becomes noisy.

2.3.3 “Subsample” covariance method: the covariance scaled from subregion area to total area

In order to develop our understanding of the nature of JK covariance, we also study another method, which we hereafter call the “subsample” covariance. We implement this method as follows. (1) Divide the survey region into N_{sub} subregions, where each subregion has an equal area as in the JK method. (2) Use different realizations of the light-cone simulations (therefore independent large-scale structures) to simulate lensing effects on source galaxies in each subregion. (3) Measure the stacked lensing profiles from each subregion, and estimate the covariance matrix from the standard deviations among the N_{sub} measurements. (4) Estimate the covariance matrix for the total area, by scaling the covariance matrix of subregions by a factor of the area ratio as

$$\mathbf{C}_{ij}^{\text{sub}} \equiv \frac{\Omega_{\text{sub}}}{\Omega_{\text{s}}} \frac{1}{N_{\text{sub}} - 1} \sum_{\beta=1}^{N_{\text{sub}}} \left[\widehat{\Delta\Sigma}_{(\beta)}(R_i) - \overline{\Delta\Sigma}(R_i) \right] \left[\widehat{\Delta\Sigma}_{(\beta)}(R_j) - \overline{\Delta\Sigma}(R_j) \right], \quad (16)$$

where Ω_{s} is the area of the survey (total area), Ω_{sub} is that of each subregion ($\Omega_{\text{s}}/\Omega_{\text{sub}} = N_{\text{sub}}$ in our setting), and $\widehat{\Delta\Sigma}_{(\beta)}(R_i)$ is the lensing profile measured from the β -th subregion, and

$$\overline{\Delta\Sigma}(R_i) \equiv \frac{1}{N_{\text{sub}}} \sum_{\beta=1}^{N_{\text{sub}}} \widehat{\Delta\Sigma}_{(\beta)}(R_i). \quad (17)$$

The difference of this method from the JK method is that the lensing profiles measured from the different subregions are independent, while the lensing fields in the JK method arise from the same realization of large scale structure covering the total area.

Besides the prefactor of $\Omega_{\text{sub}}/\Omega_{\text{s}}$ in equation (16), the estimator is similar to equation (12), thus estimating the full covariance for the subregion area. If the covariance amplitude scales with a survey area as $1/\Omega_{\text{s}}$, the covariance for the total survey area would be smaller than that of the subregion by a factor of $\Omega_{\text{sub}}/\Omega_{\text{s}}$. However, as we discussed, this scaling relation should be violated in the presence of SSC. The SSC contribution to the full covariance for subregion area arises from super-survey modes whose length scales are greater or comparable with the size of “subregion”, not total survey area. Hence by comparing the above covariance with the full covariance method in Section 2.3.1, we can quantify the relative contribution of SSC terms of the subregion and total areas. We expect the greater SSC contribution for the subregion area than that for the total area, because the variance of the super-survey modes for the subregion area is larger than that for the total area as predicted in the CDM scenario (Takada & Hu 2013). Note that, as in the JK method, a maximum separation R_{max} of the lensing profile $\Delta\Sigma(R)$ is set by the size of the subregion. This subsample covariance would be the case if different subregions are separated by a large distance on the sky such that the subregions are considered independent (no correlation between the lensing fields in different subregions)⁸.

By the analogy to clustering analysis of galaxies, one may be concerned about the integral constraint in the case of subsample covariance method. Nevertheless, the stacked shear profile, which is defined in terms of the integral of the power spectrum weighted with the 2nd-order Bessel function, $J_2(x)$ (see Eq. [5]), does not obey the integral constraint, unlike the two-point correlation function of the convergence field that involves the integral of the zero-th order Bessel function, $J_0(x)$ (e.g., see around Eq. (1) in Beltrán Jiménez & Durrer (2011)). Hence, the stacked shear profile even for the subregion method can be estimated without any problem, based on the pair counting statistics.

3 SIMULATIONS

3.1 N -body simulation

In order to study in detail the weak lensing statistics considered in this paper, we use the full-sky weak lensing maps that are constructed from multiple sets of N -body simulation realizations. N -body simulations can properly model nonlinear structure formation as well as the resulting non-Gaussianity in the distributions of halos and dark matter.

To run each cosmological N -body simulation, we used the parallel Tree-Particle Mesh code `Gadget2` (Springel 2005). We employed 2048³ N -body particles. For each N -body simulation, we generated the initial conditions using a parallel code developed by Nishimichi et al. (2009) (also see Valageas & Nishimichi 2011), which is based on the second-order Lagrangian perturbation theory (e.g. Crocce, Pueblas & Scoccimarro 2006). To set up the the initial conditions we used CAMB (Lewis, Challinor & Lasenby 2000) to compute the linear matter transfer function for the fiducial cosmological model. The fiducial model is characterized by the following cosmological parameters: the

⁸ Exactly speaking, even in this case the different subregions are correlated by super-survey modes corresponding to the separation distance, so this causes the SSC term, which should however be smaller than the SSC term of subregion area.

| $L_{\text{box}} [h^{-1}\text{Mpc}]$ | ID of lens-shells | Output redshifts | Number of realizations |
|-------------------------------------|-------------------|-----------------------|------------------------|
| 450 | 1, 2, 3 | 0.0251, 0.0763, 0.128 | 6 |
| 900 | 4, 5, 6 | 0.182, 0.237, 0.294 | 6 |
| 1350 | 7, 8, 9 | 0.352, 0.413, 0.475 | 6 |
| 1800 | 10, 11, 12 | 0.540, 0.607, 0.677 | 6 |
| 2250 | 13, 14, 15 | 0.750, 0.827, 0.906 | 6 |
| 2700 | 16, 17, 18 | 0.990, 1.077, 1.169 | 6 |
| 3150 | 19, 20, 21 | 1.267, 1.369, 1.477 | 6 |
| 3600 | 22, 23, 24 | 1.592, 1.714, 1.844 | 6 |
| 4050 | 25, 26, 27 | 1.982, 2.129, 2.287 | 6 |

Table 1. Parameters of N -body simulations, used in generating the full-sky light-cone simulations. Each simulation was run with 2048^3 dark matter particles. The output redshift of each simulation corresponds to the comoving distance to the center of lens shell. We adopted the standard CDM model, which is consistent with WMAP 9-yr results (Hinshaw et al. 2013).

density parameter of total matter $\Omega_{\text{m}0} = 0.279$, the density parameter of baryon $\Omega_{\text{b}0} = 0.046$, the density parameter of the cosmological constant $\Omega_{\Lambda 0} = 0.721$, the density fluctuation amplitude $\sigma_8 = 0.823$, the Hubble parameter $h = 0.700$ and the spectral index $n_s = 0.972$. These parameters are consistent with the nine-year WMAP results (Hinshaw et al. 2013).

To simulate large-scale structures in the light cone covering up to sufficiently high redshifts of source galaxies we are interested in, we used the N -body simulation realizations for 9 different box sizes which range from $450 h^{-1}\text{Mpc}$ to $4050 h^{-1}\text{Mpc}$, stepped by $450 h^{-1}\text{Mpc}$ in the side length. For each box-size N -body simulation, we generated 6 different realizations, each of which was run using the different initial seeds for the same cosmological model. Hence we use $54 (= 6 \times 9)$ N -body simulation realizations in total. As illustrated in Fig. 2 of Shirasaki, Hamana & Yoshida (2015), we place the N -body simulation realizations around a hypothetical observer at the coordinate origin (“O” in the left panel of Fig. 1) so as to cover the past light-cone around the observer. To cover the full sky, we repeatedly use the same realization of each box size, by placing 8 boxes of the same realization around the observer. In doing this the matter distribution in each redshift slice becomes continuous due to the periodic boundary condition. However, note that the ray-tracing simulations we use ignore the Fourier modes greater than the N -body simulation volume, which correspond to angular modes greater than $\sqrt{4\pi/8}$ radian. The largest-volume simulation with $4050 h^{-1}\text{Mpc}$ on a side enables us to simulate the lensing effect on source galaxies up to redshift $z \simeq 2.4$ for our fiducial cosmological model. While one main purpose of this paper is to generate a mock catalog of the SDSS weak lensing fields, the redshift distribution of SDSS source galaxies peaks around $z \simeq 0.5$ and has a long tail extending up to $z \sim 1$, as shown in Fig. 5 in Mandelbaum et al. (2013) (more exactly speaking the maximum photometric redshift is $z \simeq 1.49$). Thus our N -body simulations are sufficiently large to cover the entire large-scale structure in the light cone that is probed by SDSS (also see below). The further details can be found in Shirasaki, Hamana & Yoshida (2015) (also see Takahashi et al. in preparation).

3.2 Full-sky lensing simulation

We here briefly summarize our ray-tracing simulations with full-sky coverage. The detailed description is found in Appendix A of Shirasaki, Hamana & Yoshida (2015). In our ray-tracing simulation, we used the standard multiple lens-plane algorithm (e.g., Hamana & Mellier 2001) to compute the light-ray path and the lensing magnification matrix for source galaxies in different redshift slices. To take into account the curvature of the celestial sphere, we performed the multiple lens-plane algorithm on a spherical geometry using the projected matter density field given in the format of spherical shell, which is generated from N -body simulation realization output at the redshift corresponding to the distance to the shell from an observer. We used the projected matter fields in 27 shells in total, each of which was computed by projecting N -body simulation realization over a radial width of $150 h^{-1}\text{Mpc}$, in order to make the light cone covering a cosmological volume up to $z \simeq 2.4$. As described above, we used 6 different box-size N -body simulations. For each box-size simulation, we computed the projected matter fields in 3 shells of different radii (radial distances), where the projected matter field in each shell is computed from different regions of the N -body simulation output at the corresponding redshift and the largest-radius shell is inscribed to the simulation box (see Fig. 2 of Shirasaki, Hamana & Yoshida 2015). Hence, our lensing simulations can model the evolution of the density field along the line of sight with the interval of comoving $150 h^{-1}\text{Mpc}$, corresponding to the redshift width of $\sim 0.05 - 0.1$. Table 1 summarizes the redshifts of N -body simulation outputs.

In computing the projected matter fields from each N -body realization, we randomly shift and rotate the simulation box in order to avoid the same structure appearing multiple times along the same line of sight. Here we properly computed the deflection of light ray in each lens plane; we did not employ the Born approximation. We used the HEALPIX software (Górski et al. 2005) to generate the projected matter fields in pixels embedded into each of the spherical shells. The angular resolution parameter n_{side} is set to be 8192 corresponding to $\simeq 0.43$ arcmin for the pixel scale (angular resolution)⁹. In our simulation, we simulated light ray trajectories from $z = 0$ to $z \simeq 2.4$ using

⁹ For a given n_{side} , the HEALPIX software divides the full sky into $12 \times n_{\text{side}}^2$ pixels each of which has an equal area, and therefore the area of each pixel is given by $4\pi/(12 \times n_{\text{side}}^2)$.

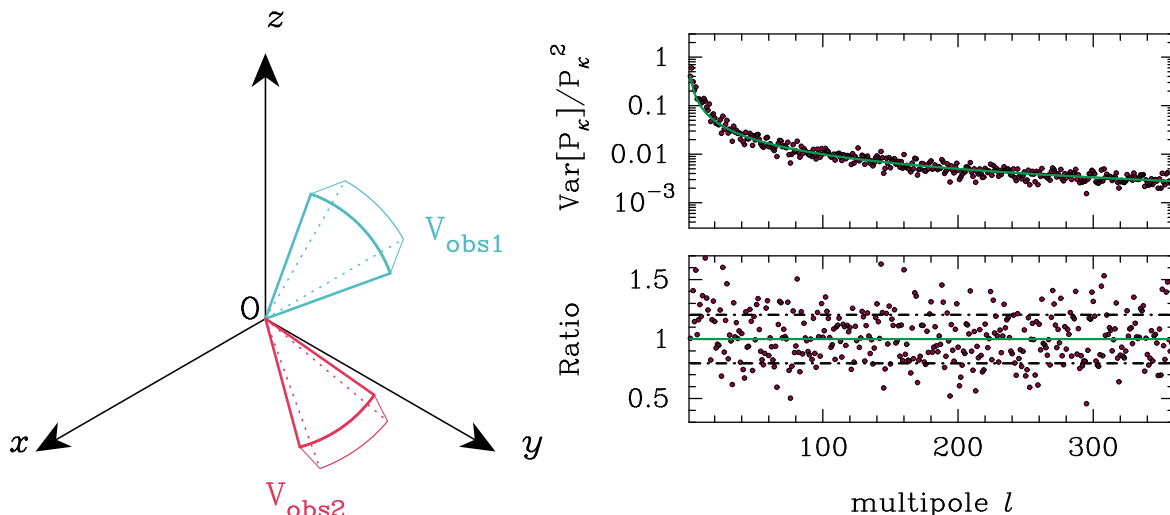


Figure 1. *Left figure:* An illustration of a galaxy survey with partial sky coverage, which has a volume of V_{obs} , in the light-cone simulation. A hypothetical observer is at the coordinate origin, O . *Right panel:* The upper plot shows the power spectrum variance for the cosmic shear convergence field, estimated from the spectra measured from the 48 full-sky lens maps. Here we consider the source redshift $z_s = 1$ and the range of low multipoles, $\ell \lesssim 360$, in the linear regime. We show the variance normalized by the average power spectrum squared, compared to the Gaussian variance $2/(2\ell + 1)$ (green curve). In the bottom panel, we show the ratio of the measured variance and the Gaussian prediction and the black dashed lines shows the expected Gaussian error of the variance, i.e., $\sqrt{2/N_{\text{rea}}}$ where $N_{\text{rea}} = 48$.

the standard multiple lens-plane algorithm. To efficiently generate mock catalogs, we stored the data of weak lensing fields (convergence and shear) in each of 26 shells for each full-sky realization. Thus the source planes are located in radial distances ranging from $150 h^{-1}\text{Mpc}$ to $4050 h^{-1}\text{Mpc}$, stepped by $150 h^{-1}\text{Mpc}$, while the lens planes are placed at a cone-volume weighted mean radial distance of each shell. In this paper, we use the weak lensing fields in 21 shells corresponding to the maximum redshift of SDSS source galaxies, $z_s \simeq 1.49$. In the following we use 48 realizations of the full-sky lensing maps that are constructed from different combinations of 54 N -body realizations (6 realizations for each of 9 different-size N -body simulations).

Our full-sky lens maps are built by using the same set of N -body simulation realizations multiple times. However, when making mock catalogs of a “partial-sky-coverage” lens map, each realization of the lensing maps is taken from the partial-solid-angle light cone around a hypothetical observer, corresponding to different subregions of N -body simulation realizations, as illustrated in Fig. 1. The mock catalogs generated from subregions of each N -body realization allow us to study the effects in galaxy-galaxy weak lensing for a finite-volume survey that is embedded in a much larger volume universe (see Li, Hu & Takada 2014a, for the similar study for three-dimensional matter power spectrum). First, the large-scale structure (N -body particle distribution) simulated in each subregion of N -body simulation realization arises from independent, linear initial density fields with length scales smaller than the subregion scale. Secondly, the matter clustering in each subregion includes mode-coupling effects with super-survey modes beyond the subregion size. As long as a volume of subregion is large enough, the super-survey modes are in the linear regime, and therefore the different subregions are affected by independent super-survey modes. Thus our simulated mock catalog mimics what we observe for an actual survey. If mock catalogs are generated from N -body simulations with periodic boundary conditions (i.e. without super-survey modes), the mock catalogs do not include the effects of super-survey modes.

We consider that the different realizations of our full-sky lens maps are nearly independent for the following reason. As we stated, we generate the different full-sky lens maps based on the multiple lens plane algorithm, where we project the three-dimensional N -body particle distribution to each lens shell along the line-of-sight direction, after performing random translation and rotation of each N -body realization. Since the lensing fields arise from Fourier modes perpendicular to the line-of-sight direction, the random translation and rotation effectively allow us to make independent realizations (Hamana & Mellier 2001). Thus in this way we can construct many, nearly independent realizations of the full-sky lens maps from different combinations of 54 different-box N -body simulation realizations. As a justification of independence of the full-sky maps, in the right panel of Fig. 1 we examine the cosmic shear power spectrum, $P_\kappa(\ell)$, for source redshift at $z_s = 1$ and in the multipole range of $\ell \lesssim 360$ from each full-sky realization, where the low multipole range is considered to be in the linear regime. Then we estimate its covariance matrix from the 48 full-sky realizations. The figure shows that the variance of P_κ is consistent with the Gaussian prediction of $\text{Var}(P_\kappa) = 2P_\kappa^2/(2\ell + 1)$ (we took $\Delta\ell = 1$ in this calculation). Furthermore, the scatters in the variance are also found to be close to the Gaussian prediction of $\sqrt{2/N_{\text{rea}}}\text{Var}(P_\kappa)$ where $N_{\text{rea}} = 48$ (Taylor, Joachimi & Kitching 2013). These results support that our full-sky lens maps can be regarded as quasi-independent realizations. Furthermore, when considering a lensing survey with a partial sky coverage, we can construct the different realizations by clipping a finite solid-angle light cone from the full-sky map along different line-of-sight directions from the observer (see the left illustration of Fig. 1), where the different realizations are from different subvolumes of the original N -body simulations in the light cone. Thus, we can further increase the number of independent realizations.

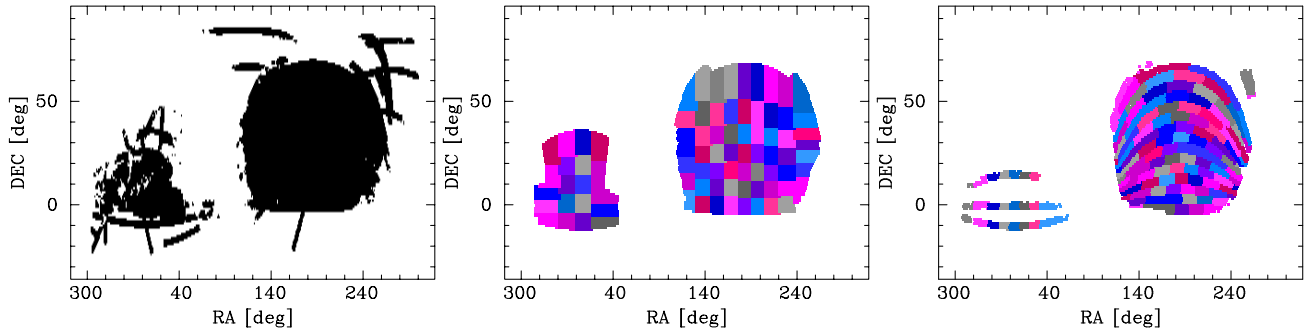


Figure 2. The survey footprints of the SDSS data used in this paper. *Left panel:* The footprints of the source galaxies constructed from the SDSS imaging data (Reyes et al. 2012), which we use for the weak lensing measurements. *Middle:* The footprints of redMaPPer clusters (Rykoff et al. 2014; Rozo et al. 2015b), which we use as tracers of large-scale structure for the stacked lensing measurements. The different color regions denote 83 roughly-equal-area subregions used for the jackknife covariance estimation, following the method in Miyatake et al. (2016b). *Right:* The footprints of luminous red galaxies (LRGs) which we use as another large-scale structure tracers for the galaxy-galaxy weak lensing measurements. The different color regions denote 100 subregions for the jackknife covariance estimation following Mandelbaum et al. (2013).

3.3 Full-sky halo catalog

In order to simulate the stacked lensing, i.e. galaxy- or cluster-shear cross-correlations, we also need a mock catalog of lensing halos that host galaxies and/or clusters we can observe from real data. We implemented the software `Rockstar` (Behroozi, Wechsler & Wu 2013) to each output of N -body simulation in the post processing, where `Rockstar` identifies dark matter halos from a clustering of dark matter particles in phase space. Throughout this paper, we define the halo mass by using the spherical overdensity criterion: $M_{200m} = 200\bar{\rho}_{m0}(4\pi/3)R_{200m}^3$, where $\bar{\rho}_{m0}$, the present-day mean mass density, is due to our use of the comoving coordinates. For redshifts $z_1 \lesssim 0.5$ relevant for lensing galaxies/clusters, our N -body simulations allow us to resolve dark matter halos with masses greater than a few times $10^{12} h^{-1} M_{\odot}$ with more than 50 N -body particles. In the following we use only “host” halos and do not use subhalos. We believe that this does not affect our results, because the main goal of this paper is to study the nature of the covariance matrix of galaxy-galaxy weak lensing in the sample variance limited regime that is in the two-halo term regime. We again use the `HEALPIX` to assign the position of each dark matter halo to the pixels in the celestial sphere. Although we used the halo catalogs at output redshift corresponding to each shell of the projected density fields ($150, 300, \dots, 4050 h^{-1} \text{Mpc}$ stepped by $150 h^{-1} \text{Mpc}$ as given in Table 1), we used the radial distance of each halo from an observer to assign the corresponding redshift to the halo, assuming the fiducial cosmological model. However, this redshift information is a small effect, and we checked that the following results are not changed even if we use the redshift of lens plane for all halos residing in the same lens slice.

3.4 Generating the mock catalogs of galaxy-galaxy weak lensing

In this section, we describe the details of creating mock catalogs for galaxy- or cluster-shear cross-correlations with full-sky simulations in Section 3.2 and 3.3. Our primary focus is to demonstrate how we can use the full-sky simulations to perform mock observations of stacked lensing in the currently-available largest sky surveys, the Sloan Digital Sky Survey (SDSS; York et al. 2000), which covers about one-quarter of the sky. Our mock catalogs are generated by combining the real catalog of source galaxies in the SDSS, the full-sky ray-tracing simulations and the halo catalogs. The computation procedures are summarized as follows:

- Take the real catalog of source galaxies, where each galaxy contains information on the position (RA and dec), shape, redshift and the lensing weight. Populate each source galaxy into one realization of our light-cone simulations according to its angular position and redshift. Thus our method maintains the observed distribution of source galaxies on the sky, their shapes as well as their redshift distribution.
- Randomly rotate ellipticity of each source galaxy to erase the real lensing signal.
- Simulate the lensing distortion effect on each source galaxy by adding the lensing contribution at each foreground lens plane, weighted by the lensing efficiency $\Sigma_{\text{cr}}(z_1, z_s)$, to the intrinsic shape.
- Identify halos that are considered to host galaxy clusters or galaxies, the redMaPPer clusters or the Luminous Red Galaxies (LRGs) in this paper, in the light-cone coordinates (redshift and angular position of each halo).
- Make hypothetical measurements of cluster- or galaxy-shear cross-correlations following exactly the similar method used in the actual measurements.

In the following we describe details of the SDSS shape catalog and the mock catalogs of the redMaPPer clusters and LRGs.

3.4.1 SDSS shape catalog

To model source galaxies, we use the shape catalog that was constructed in Reyes et al. (2012) from the SDSS DR8 photometric data (Aihara et al. 2011). In this catalog, the galaxy shapes are measured by the re-Gaussianization technique (Hirata & Seljak 2003), and the systematic

uncertainties involved in the shape measurements have been investigated in detail (Mandelbaum et al. 2005). In this catalog the inverse variance weight, w_s , is assigned to each source galaxy as

$$w_s = \frac{1}{\sigma_\epsilon^2 + \sigma_{\text{SN}}^2}, \quad (18)$$

where σ_ϵ is the estimated shape measurement error and σ_{SN} represents the rms intrinsic ellipticity, for which we throughout this paper employ $\sigma_{\text{SN}} = 0.365$ according to the result in Reyes et al. (2012). Note that, when computing the stacked lensing, we further include the lensing efficiency for the weight, $\Sigma_{\text{cr}}(z_l, z_s)$ for each source-lens pair, as given in equation (8). Following Mandelbaum et al. (2013), we use the maximum-likelihood mode of ZEBRA and choose the best-fitting photo- z , after marginalizing over the SED template, for each source galaxy redshift. As described in detail in Reyes et al. (2012) (Mandelbaum et al. 2013), we use 39,267,029 source galaxies in total, that remain after the carefully-tuned selection based on the imaging quality, data reduction quality, galactic extinction, apparent magnitude, photometric redshift and galaxy size.

To simulate weak lensing effects on the SDSS source galaxies, we use the similar method developed in Shirasaki & Yoshida (2014). In doing this, we keep all the characteristics of the SDSS data; the angular positions, the redshift and ellipticity distributions, and the survey geometry.

We first assign the celestial coordinates (RA and dec) to the full-sky simulation map. Then we populate the SDSS source galaxies in the full-sky map as follows. (1) We assign each source galaxy to the redshift of the nearest source plane from its photometric redshift, and then assign the galaxy to the nearest pixel in the source plane (the pixel scale is about $0.43'$). Note that, as we described, our source planes are discrete and located in the radial distances starting from $150 h^{-1}\text{Mpc}$ up to $4050 h^{-1}\text{Mpc}$, stepped by $150 h^{-1}\text{Mpc}$, corresponding to the redshift width of $\Delta z \simeq 0.05$. Since this redshift width is smaller than a typical error of the photometric redshifts of SDSS galaxies (by a factor of 2) (Nakajima et al. 2012), we believe that the assignment procedure of source redshifts would be accurate enough. More exactly speaking we can further include the probability distribution of photo- z for each galaxy in the redshift assignment, but we ignore this for simplicity in this paper. (2) For each galaxy we randomly rotate the ellipticity orientation to erase the real lensing signal. Since the intrinsic ellipticity is larger than the lensing effect on individual galaxy basis, we can approximate the intrinsic ellipticity, ϵ_{int} , by the observed ellipticity. We should note that the ellipticity of the shape catalog in Reyes et al. (2012) is defined in terms of the *distortion* (Miralda-Escude 1991; Bernstein & Jarvis 2002), whose amplitude is related to the major and minor axes of an ellipse as $(a^2 - b^2)/(a^2 + b^2)$. (3) We then simulate the lensing distortion effect on each galaxy. As we described, we have the lensing fields as a function of the angular position (RA and dec) and source plane redshift. Using the matrix multiplication rule, we can simulate the ‘‘observed’’ ellipticity, denoted as ϵ_{mock} , for each galaxy by adding the intrinsic ellipticity and the simulated lensing effect:

$$\epsilon_{\text{mock},1} = \frac{\epsilon_{\text{int},1} + \delta_1 + (\delta_2/\delta^2)[1 - (1 - \delta^2)^{1/2}](\delta_1\epsilon_{\text{int},2} - \delta_2\epsilon_{\text{int},1})}{1 + \boldsymbol{\delta} \cdot \boldsymbol{\epsilon}_{\text{int}}}, \quad (19)$$

$$\epsilon_{\text{mock},2} = \frac{\epsilon_{\text{int},2} + \delta_2 + (\delta_1/\delta^2)[1 - (1 - \delta^2)^{1/2}](\delta_2\epsilon_{\text{int},1} - \delta_1\epsilon_{\text{int},2})}{1 + \boldsymbol{\delta} \cdot \boldsymbol{\epsilon}_{\text{int}}}, \quad (20)$$

where $\boldsymbol{\delta} \equiv 2(1 - \kappa)\boldsymbol{\gamma}/[(1 - \kappa)^2 + \gamma^2]$ and κ and $\boldsymbol{\gamma}$ are the lensing convergence and shear fields, respectively. Note $\boldsymbol{\delta} \simeq 2\boldsymbol{\gamma}$ in the weak lensing regime.

Thus our mock source galaxies preserve the observed angular positions, redshifts, intrinsic ellipticities and lensing weights of real galaxies, while we properly simulate the ellipticity of galaxies by combining the lensing distortion extracted from ray-tracing simulations with the intrinsic ellipticity for individual galaxies. The intrinsic ellipticities give a dominant source of the statistical errors in the stacked lensing at small scales, so using the observed information of source galaxies is crucial to reproduce the statistical errors at the small scales as we will show below.

3.4.2 Clusters of galaxies – redMaPPer clusters

The stacked lensing analysis requires to use tracers of large-scale structure at lens redshift. As one kind of tracers, we use the publicly available catalog of galaxy clusters, the red-sequence Matched-filter Probabilistic Percolation (redMaPPer) catalog (Rykoff et al. 2014), constructed based on the SDSS DR8 photometric galaxy catalog. The redMaPPer algorithm identifies clusters of galaxies as overdensities of red-sequence galaxies at similar redshift by using the *ugriz* magnitudes and their errors. For each cluster, the catalog contains an optical richness estimate λ , a photometric redshift estimate z_λ , as well as the position and probabilities of 5 candidate central galaxies. In this paper, we utilize the catalog created by v5.10 version of the algorithm with various improvements (see Rozo et al. 2015b, for details). This is the same catalog as used in Miyatake et al. (2016b), which consists of an approximately volume-limited sample of 8,648 redMaPPer clusters with $20 < \lambda < 100$ and $0.1 < z_\lambda < 0.33$.

In order to create the mock catalog of redMaPPer clusters, we need to model the relation between the observed optical richness and halo mass, which allows us to assign halos in the simulations to hypothetical redMaPPer clusters. We adopt the relation derived in Simet et al. (2016). They assumed a log-normal distribution $P(\ln M|\lambda)$, which describes the probability distribution of cluster masses $\ln M$ for a given richness λ , and then calibrated the mean relation $\langle M|\lambda \rangle$ using the weak lensing measurements for the 4 subsamples divided by different

ranges of richness λ :

$$\langle M|\lambda \rangle = 10^{14.344} [h^{-1}M_{\odot}] \left(\frac{\lambda}{40} \right)^{1.33}. \quad (21)$$

We also adopt the model variance in $\ln M$ as a function of richness, derived in [Simet et al. \(2016\)](#):

$$\text{Var}(\ln M|\lambda) = \frac{1.33^2}{\lambda} + \sigma_{\ln M|\lambda}^2, \quad (22)$$

where the intrinsic scatter $\sigma_{\ln M|\lambda}$ is fixed to be 0.25 according to [Roza & Rykoff \(2014\)](#) (also see [Roza et al. 2015a](#)). Convolving the observed number counts of clusters with the above probability distribution between halo mass and optical richness, we can infer the underlying halo mass function in the SDSS area:

$$F^{\text{RM}}(\ln M) = \frac{1}{N_{\text{tot}}^{\text{RM}}} \int_0^{\infty} d\lambda \frac{dN^{\text{RM}}}{d\lambda} P(\ln M|\lambda), \quad (23)$$

where $(dN^{\text{RM}}/d\lambda) d\lambda$ is the observed number counts of redMaPPer clusters in the richness bin $[\lambda, \lambda + d\lambda]$, $N_{\text{tot}}^{\text{RM}}$ is the total number of redMaPPer clusters (i.e. $N_{\text{tot}}^{\text{RM}} = 8,648$), and $F^{\text{RM}}(\ln M)$ is a fraction of the underlying halo candidates hosting redMaPPer clusters in halo mass bin $[M, M + d \ln M]$ relative to the total number of redMaPPer clusters.

We employ the following approach to create a mock catalog of redMaPPer clusters in each realization of our full-sky, light-cone simulations. (1) We identify candidate halos in the simulation realization that have $M_{200\text{m}} \geq 10^{13} h^{-1} M_{\odot}$ and are in the range of $0.1 < z < 0.33$, and then compute the fractional mass function $F^{\text{sim}}(\ln M)$, which is a fraction of halos in mass bin $[M, M + d \ln M]$ among all the selected halos. Since the range of halo masses in the simulation is different from that in the redMaPPer clusters, we renormalize the mass function $F^{\text{sim}}(\ln M)$; we multiply $F^{\text{sim}}(\ln M)$ by an overall constant factor so as to match the observed mass function, $F^{\text{RM}}(\ln M)$, at high mass ends, $M_{200\text{m}} \gtrsim$ a few $10^{14} h^{-1} M_{\odot}$. (2) If $F^{\text{RM}}(\ln M) \geq F^{\text{sim}}(\ln M)$ in a halo mass bin $[M, M + d \ln M]$, we select all the halos as hypothetical redMaPPer clusters. If $F^{\text{RM}}(\ln M) < F^{\text{sim}}(\ln M)$, we make a random downsampling of halos in the mass bin. (3) We also assign a hypothetical richness to each selected halo assuming the probability $P(\lambda|\ln M) \propto P(\ln M|\lambda)(dN^{\text{RM}}/d\lambda)$ such that the selected halos with assigned richness reproduce the observed richness function, $dN^{\text{RM}}/d\lambda$. (4) We then compute the “normalized” radial distribution of mock halos, $(1/N_{\text{tot}}^{\text{sim}})dN^{\text{sim}}/d\chi$, in 20 discrete radial bins in the range of $0.1 < z < 0.33$ via the redshift-distance relation $\chi(z)$ for the fiducial cosmological model. If the probability of mock clusters in a given radial bin is greater than that of real redMaPPer clusters, we made a random downsampling of mock clusters at the bin by the ratio. For the random catalogs of redMaPPer clusters, we used 20 realizations of the random catalog that are used for the stacked lensing measurements from the mock catalogs (see equation 7).

Next we define the survey footprints of SDSS data in the light-cone simulation by using the randoms catalog of the redMaPPer clusters (version 5.10 at the url <http://risa.stanford.edu/redmapper/>). To do this, we assign, to each full-sky simulation, the `HEALPIX` pixels with angular resolution parameter $n_{\text{side}} = 512$ corresponding to angular resolution of about 6.8 arcmin, which is a coarse-grained pixelization of our default pixel scale ($n_{\text{side}} = 8192$ corresponding to 0.43 arcmin). Since our full-sky simulation is given in the hypothetical RA and dec coordinates (see Section 3.4), we can assign each random point of the redMaPPer catalog to the nearest `HEALPIX` pixel. By identifying the pixels that contain at least one random point, we define the survey footprints in the full-sky simulation. However, note that our method does not account for the smaller-scale masks such as those due to bright stars and does not consider other observational effects such as variations in the survey depth that might affect the selection of redMaPPer clusters in the real data. The middle panel in Fig. 2 shows the effective area of the redMaPPer catalog. We then select the hypothetical redMaPPer clusters that reside within the defined survey footprints in each simulation realization. After these selection procedures, the total number of mock clusters is typically greater than that of the real clusters (8,648) by 10–20%, probably because we do not account for a redshift evolution in the optical richness and halo mass relation and/or do not consider observational effects such as the small-scale masks. Hence, we further make a random downsampling of the mock clusters by the ratio of the total numbers of mock and real clusters. Since the shear-cluster cross-correlation probes the *average* mass distribution around the sampled clusters, the estimator does not largely depend on the selection of clusters or the total number of clusters in the sample (equation 7). Note that our approach of making a mock catalog of redMaPPer clusters is different from the forward modeling method, where the observed richness function is modeled by convolving the theoretical halo mass function with the probability function $P(\lambda|\ln M)$ that gives a probability distribution of richness for a given halo mass M including the scatters in λ ([Lima & Hu 2005](#); [Oguri & Takada 2011](#)) (also see [Murata et al. in preparation](#)). Since the main purpose of this paper is to study the covariance for the stacked lensing, we believe that our mock catalog is accurate enough, as we will show below in detail.

As we described, the source galaxies in the mock catalog (see Section 3.4.1) include simulated lensing distortion due to the mass distribution in the lens plane containing the mock clusters. Hence, by taking the cross-correlation between the positions of the mock redMaPPer clusters with the shapes of source galaxies, we can perform a mock measurement of the stacked lensing. Note that we do not consider an off-centering effect for simplicity; we use the true halo center for the stacked lensing measurement in the mock catalogs, as our main focus is to study the covariance at large scales. When implementing the JK method in the mock catalog, we use the same subdivision of survey footprints as in [Miyatake et al. \(2016b\)](#), including 63 and 20 for the northern and southern hemisphere footprints, respectively (see the middle panel of Fig. 2). The different realizations of the full maps contain different realizations of mock clusters and large-scale structure, and allow us to estimate the full covariance.

3.4.3 Massive galaxies – Luminous Red Galaxies

We also consider another useful tracers of large-scale structure, the sample of luminous red galaxies (LRGs) (Eisenstein et al. 2001; Wake et al. 2006), which was constructed from the SDSS DR7 data and made publicly available in Kazin et al. (2010). The selection of LRGs are based on their color and magnitude and well-designed to make the resulting sample be approximately volume-limited out to $z \simeq 0.36$. In this paper, we use the same sample of LRGs as in Mandelbaum et al. (2013), which consists of 62,081 LRGs with g -band absolute magnitude $-23.2 < M_g < -21.2$ in the redshift range of $0.16 \leq z < 0.36$. The LRGs are early-type, bright galaxies and thought to reside in halos with a few $10^{13} h^{-1} M_\odot$ that are less massive than the redMaPPer clusters.

In order to create the mock catalog of LRGs, we employ the halo occupation distribution (HOD) method that allows us to populate hypothetical LRGs into halos in the simulations. The HOD, denoted by $\langle N_{\text{gal}}|M \rangle$, gives the mean number of galaxies in host halos with mass M . Following the method in Zheng et al. (2005), we employ the HOD model with the form given by

$$\langle N_{\text{gal}}|M \rangle = \langle N_{\text{cen}}|M \rangle (1 + \langle N_{\text{sat}}|M \rangle), \quad (24)$$

with

$$\langle N_{\text{cen}}|M \rangle = \frac{1}{2} \left[1 + \text{erf} \left(\frac{\log M - \log M_{\text{min}}}{\sigma_{\log M}} \right) \right], \quad (25)$$

$$\langle N_{\text{sat}}|M \rangle = \left(\frac{M - M_{\text{cut}}}{M_1} \right)^\alpha \Theta(M - M_{\text{cut}}), \quad (26)$$

where $\langle N_{\text{cen}}|M \rangle$ denotes the HOD of central galaxies, $\langle N_{\text{sat}}|M \rangle$ is the contribution of satellite galaxies and $\Theta(x)$ is the Heaviside step function. In this paper, we adopt the model parameters derived in Reid & Spergel (2009): $(M_{\text{min}}, \sigma_{\log M}, M_{\text{cut}}, M_1, \alpha) = (5.64 \times 10^{13} h^{-1} M_\odot, 0.7, 3.50 \times 10^{13} h^{-1} M_\odot, 3.47 \times 10^{14} h^{-1} M_\odot, 1.035)$. We do not consider the redshift evolution of the HOD parameters.

Similarly to the redMaPPer catalog, we populate hypothetical LRGs in halos in the range of $0.16 \leq z < 0.36$ for each realization of the light cone simulations. (1) We populate central LRGs into halos by randomly selecting halos according to the probability distribution, $\langle N_{\text{cen}}|M \rangle$ (equation 25). We assume that each central LRG resides at the halo center. (2) For the halos that host the central LRG, we randomly populate satellite LRG(s) assuming a Poisson distribution with the mean $\langle N_{\text{cen}}|M \rangle \langle N_{\text{sat}}|M \rangle$. We assume that the radial distribution of satellite LRGs on average follows that of dark matter in each host halo. Here we assume the analytical NFW profile (Navarro, Frenk & White 1997) for simplicity, where we use the halo mass and the scale radius, measured by the `Rockstar`, to compute the NFW profile for each host halo. Then we compute the normalized radial distribution of mock LRGs in the discrete 20 bins in the range of $0.16 \leq z < 0.36$. If the probability of mock LRGs in a given bin is greater than that of the real LRGs, we made a random downsampling of mock LRGs so as to match the radial distribution. To make a mock measurement of galaxy-galaxy lensing for the mock catalog of LRGs, we used 10 realizations of the random catalog.

Next, by comparing the random catalog with the simulated sky map in the `HEALPIX` format of angular resolution parameter $n_{\text{side}} = 256$ (corresponding pixel size of about 13.6 arcmin), we define the survey footprints of the LRG catalog. The survey footprints of the LRG catalog is shown in the right panel of Fig. 2. We then select the hypothetical LRGs in each simulation that resides within the defined survey footprints. After these procedures the total number of mock LRGs is found to be close to the real number (62,081) with the scatter of ~ 100 . When estimating the covariance in the JK method, we use the same subdivision of the area into 100 subregions in Mandelbaum et al. (2013), as explicitly shown in the right panel of Fig. 2.

4 RESULTS

4.1 Numerical tests of the covariance of stacked lensing

Before going to the results for the mock catalogs of SDSS redMaPPer clusters and LRGs, we first study the different covariance estimators of stacked lensing profile using our light-cone simulations (lensing fields as well as halo catalog), but not using the SDSS source galaxy catalog for now. For this purpose, we consider a sample of mass-limited halos with $M \geq 10^{13.5} h^{-1} M_\odot$ and in the redshift range $z = [0.10, 0.27]$. This sample typically contains $\sim 180,000$ halos over one full-sky simulation. For the following results we use 10 realizations of the random catalogs. For source redshift, we simply consider a single source plane at $z_s = 0.5$, distributed on the regular grids (about 0.43 arcmin for grid scale), and will not consider the intrinsic ellipticity or shape noise contamination to the covariance unless otherwise stated. The main purpose of the numerical experiments is to understand the nature of the JK covariance estimator in terms of the SSC effect. For a reader who is more interested in the results for the SDSS mock catalogs, please skip to Section 4.2.

4.1.1 Comparison of the covariance estimators: full covariance vs. jackknife covariance

We first compare the different covariance estimators using the simulation realizations each of which has the same total area, $\Omega_s \simeq 859$ sq. degrees, corresponding to $f_{\text{sky}} = 1/48$ for the sky fraction. Since our simulation maps are all given in the `HEALPIX` pixelization, we

| | Sky fraction f_{sky} | Number of subregions | Number of realizations |
|---------------|---|----------------------|------------------------|
| S859-full | $f_{\text{sky}} = 1/48$ (859.4 sq. degs) | – | 480 |
| S859-jk1/sub1 | $f_{\text{sky}} = 1/48$ (859.4 sq. degs) | 12 | 480 |
| S859-jk2/sub2 | $f_{\text{sky}} = 1/48$ (859.4 sq. degs) | 64 | 480 |
| S859-jk3/sub3 | $f_{\text{sky}} = 1/48$ (859.4 sq. degs) | 256 | 480 |
| S3437-full | $f_{\text{sky}} = 1/12$ (3437 sq. degs) | – | 120 |
| S215-full | $f_{\text{sky}} = 1/192$ (214.8 sq. degs) | – | 1920 |
| S54-full | $f_{\text{sky}} = 1/768$ (53.71 sq. degs) | – | 7680 |

Table 2. Summary of the parameters of simulations used for the comparison of different covariance estimators for numerical experiments of galaxy-galaxy weak lensing for a sample of mass-selected halos with $M_{200\text{m}} \geq 10^{13.5} h^{-1} M_{\odot}$ and in the redshift range $z_1 = [0.1, 0.27]$. The different columns denote the sky coverage (f_{sky}) of each simulation realization, whether the covariance is estimated with or without subdivision of each realization, and the number of realizations, for each experiment.

define the hypothetical survey footprint with $f_{\text{sky}} = 1/48$ by one pixel of the `HEALPIX` pixelization with $n_{\text{size}} = 2^{10}$. For comparison purpose, we use exactly the same realizations of the hypothetical surveys when comparing the different covariance estimators: we construct 480 realizations (each of which has $f_{\text{sky}} = 1/48$) from our full-sky simulation realizations. To perform the JK covariance estimation, we further subdivide each survey footprint by the finer pixelization of `HEALPIX`, 12, 64, 256 subdivisions, respectively. Table 2 summarizes the survey realizations, named as “S859-X”, where “X” is either “full”, “jk” or “sub” denoting either the full, jackknife or subsample covariance estimator in Sections 2.3.1, 2.3.2, or 2.3.3, respectively.

The upper panel of Fig. 3 shows the surface excess mass density profile, $\Delta\Sigma(R)$, computed from the average of 480 realizations of the mock catalog of mass-limited halos with $M_{200\text{m}} \geq 10^{13.5} h^{-1} M_{\odot}$. We employ 15 equally-spaced logarithmic bins with the bin width of $\Delta \ln R = 0.31$ in the range of $1.5 < R [h^{-1} \text{Mpc}] < 178$. The expectation value of stacked lensing probes the average mass distribution around the lensing halos as a function of centric radii, and we confirmed that the sufficient number of realizations gives a well-converged value at each radial bin. For comparison, the solid curve is the analytical halo model prediction, where we employed the same model ingredients in Hikage et al. (2013); the model ingredients are the NFW profile for the halo mass density profile and the fitting formulas for the mass function and the halo bias (Tinker et al. 2008, 2010). The analytical model shows a 10-20%-level agreement with the simulation results over the range of radii. The agreement validates an accuracy of the N -body simulations and halo catalogs we are using in this paper. The error bars at each bin are estimated from the diagonal components of the full covariance, estimated from the standard deviation of 480 realizations, denoted as “S859-full” in Table 2. Although we did not include the shape noise, the error covariance arises from various contributions: a shot noise due to a finite number of lensing halos, the sample variance of mass distribution in the lens planes, the projection effect of large-scale structure along the same line of sight out to sources at $z_s = 0.5$, and the SSC contribution.

The lower panel compares the different covariances estimated based on the full covariance method (square), the JK method (blue circle) or the subsample method (green circle). Note that we used exactly the same 480 realizations of mock catalogs to estimate the different covariances. For the JK and subsample methods, we estimate the covariance matrix in each realization. The bold lines connected by the circle symbols are the average of 480 covariance matrices, and the shaded region around the lines show the 10-90% distribution in the 480 measurements. We confirmed that the subtraction of the signals around random points (the 2nd term in equation 7) is important for the covariance estimation, as claimed in Singh et al. (2016). While including the 2nd term in the estimator changes the signal by up to a few 10% in the amplitude at the large scales up to $\sim 100 \text{Mpc}/h$, it reduces the variance amplitudes by up to a factor of 2. The amount of the reduce by the random subtraction is larger in the order of the subsample, JK and full covariance methods. The random subtraction corrects for the cosmic shear contribution due to a general survey geometry, as implied by the last term of equation (10) in Singh et al. (2016); the random correction is not needed for the halo-matter cross-correlation estimation if a geometry obeys periodic boundary conditions, e.g. as in N -body simulation box, although it is not realized in an actual observation. We should note that, if we do not employ the random subtraction, the variances for the JK and subsample methods are larger than that of the full covariance method.

The lower panel shows that, at radii $R \lesssim 6 h^{-1} \text{Mpc}$, all the covariance matrices agree with each other on average, implying that each method gives an unbiased estimation of the error bars. The error bars at the small separations arise mainly from the Gaussian term (and the non-Gaussian term of sub-survey modes, although seems subdominant), because the term scales with the number of pairs used in the stacked lensing measurement at each separation bin; $[\text{Var}(\Delta\Sigma)]^{1/2} \propto 1/\sqrt{N_{\text{pair}}} \propto 1/[\Omega_s R^2]^{1/2}$ for logarithmically spacing bins. At the larger separations $R \gtrsim 6 h^{-1} \text{Mpc}$, the JK method is in good agreement with the full covariance method at a level of 10% in the amplitude, while the subsample method appears to under-estimate the error. We should note that the JK and subsample variances have a scatter and are therefore noisy in each realization basis.

We also compare the JK methods of different subdivisions for a fixed total area ($f_{\text{sky}} = 1/48$) in the left panel of Fig. 4. Here we consider the JK results for 12, 64 and 256 subdivisions corresponding to 72, 13, and 3.4 sq. degrees for each subregion, respectively. Again notice that we used exactly the same 480 realizations for the covariance estimations. To compute the JK covariance we remove only the lensing halos in each subregion for the JK resampling as done in the actual measurements (e.g., Mandelbaum et al. 2013).

¹⁰ See <http://healpix.sourceforge.net> for detail of the `HEALPIX` pixelization.

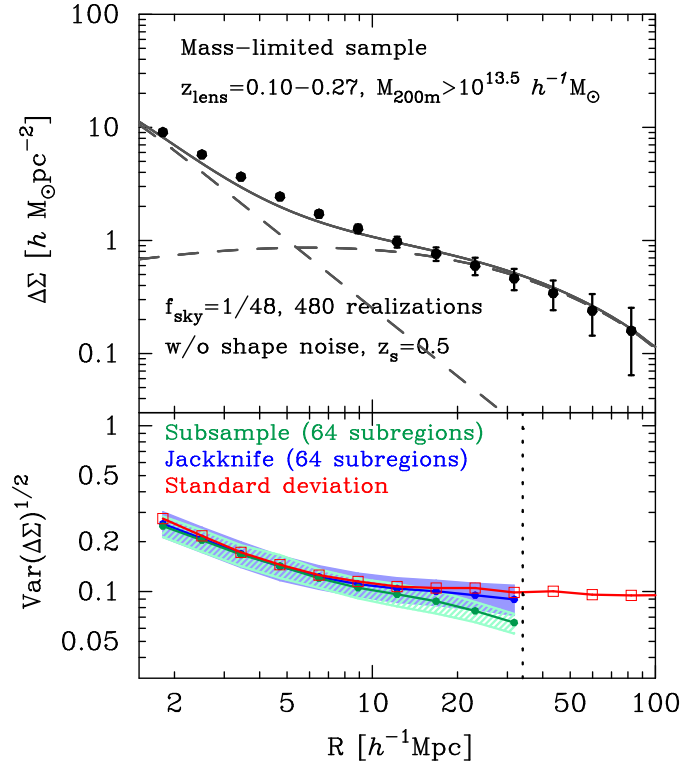


Figure 3. A simulation of the galaxy-galaxy weak lensing for a hypothetical survey with survey area $\Omega_s \simeq 859$ sq. degrees corresponding to the sky fraction of $f_{\text{sky}} = 1/48$. We consider, as lensing objects, a sample of mass-limited halos with $M_{200\text{m}} \geq 10^{13.5} h^{-1} M_{\odot}$ in the redshift range of 0.10 – 0.27 (see text for details). As for source galaxies we assume that all the galaxies are at a single redshift $z_s = 0.5$ for simplicity, and are regularly distribution in grids spaced by 0.43 arcmin (corresponding to the number density $\bar{n}_s \simeq 5.4 \text{ arcmin}^{-2}$). We do not consider the intrinsic shapes. Note that the simulated lensing effect on each source galaxy includes not only the mass contribution in the lens planes, but also the mass contribution along the line of sight at different redshifts, i.e. the projection effect. For this study we use the 480 realizations of mock simulations (halo catalogs and source galaxies). *Upper panel:* The black points show the average signal over the 480 realizations, while the error bars are estimated from diagonal components of the full covariance matrix, i.e. the standard deviation of the 480 measurements. For comparison, the solid and dashed curves show the analytical, halo model predictions (see text for details). *Lower panel:* Comparison of the different covariance estimators, the jackknife, subsample and full covariance methods, in Section 2.3. The open square symbols, connected by the red line, show the diagonal components of the full covariance at each separation bin. On the other hand, the blue and green circles are the results for the jackknife and subsample methods; the covariance of each method is estimated from each realization, the circles are the average of the 480 covariance matrices, and the shaded regions around the curve show the 10-90% range of distribution in the 480 measurements. All the covariance estimations include the subtraction of the random signals. The vertical dotted line denotes the projected length corresponding to the size of each subregion at the lens redshift. For these results we used 10 realizations of the random catalogs of lensing halos for each of the lens map realizations (see equation 7).

Fig. 4 shows that all the covariance estimators including the full covariance are in fairly nice agreement with each other at small separations on average, as we found in Fig. 3. The JK variances are in nice agreement with the full variance at radii up to the size of JK subregion, to within about 10% in the amplitude for different subdivisions. At the larger separations, the curve starts to decrease, i.e. under-estimating the true covariance, by a larger amount at the larger radii. This is because the stacked lensing measurements at separations greater than the JK subregion are in less variations between the different JK resamples for a given realization. In Appendix A, we show the off-diagonal terms of JK covariance as in Figure 4. We found that the off-diagonal term is less sensitive to the number of JK subregions once it is normalized by the diagonal term.

The right panel of Fig. 4 shows the covariance matrices for the subsample method using the same subdivisions of total area as in the JK method in the left panel. We again notice that, in this method, we use different realizations of the light-cone simulations to generate the lensing fields and lensing halos in each subregion, and there is no correlation between the lensing fields in different subregions. Except for the amplitude, the subsample method shows a similar scale dependence of the covariance to what is found in the JK method up to the separation scale corresponding to the projected size of subregion. The overall difference among three cases in the right panel can be partly explained by the averaging effect of the subsample variance over different realizations. Since the variance at small radii should be scaled with $1/N_{\text{pair}}$, the averaged subsample variance over realizations induces the difference between $\langle 1/N_{\text{pair}} \rangle$ and $1/\langle N_{\text{pair}} \rangle$. The factor of $\Omega_{\text{sub}}/\Omega_s$ in equation (16) is intended to correct for the difference of $\langle N_{\text{pair}} \rangle$ between the area of total survey region and the subregion. We find the difference between $\langle 1/N_{\text{pair}} \rangle$ and $1/\langle N_{\text{pair}} \rangle$ over 480 realizations by 3%, 10% and 30% for 12, 48, and 256 subdivisions respectively. Once we include these differences, the subsample method can show a reasonably good fit to the true covariance at $R < 10 h^{-1} \text{Mpc}$. The tendency of $\langle 1/N_{\text{pair}} \rangle \langle N_{\text{pair}} \rangle \neq 1$ should be more prominent for a smaller sky coverage. We confirmed that the difference arises from the sample variance in the number of lensing halos, a sort of the super sample variance effect, as first pointed out in Hu & Kravtsov (2003).

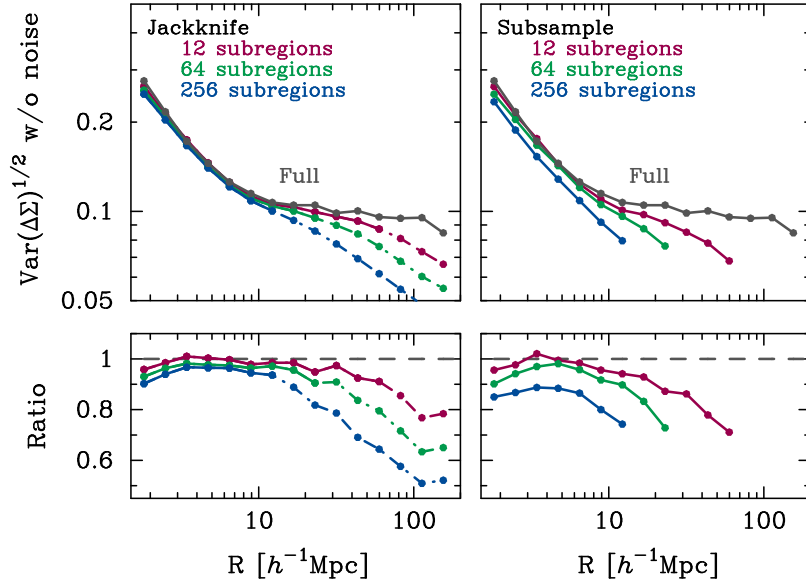


Figure 4. *Left panels:* The dependence of the jackknife covariances on different subdivisions. For comparison we used the same 480 realizations as in Fig. 3, each of which has an area of 859 sq. degrees ($f_{\text{sky}} = 1/48$). We make different subdivisions, 12, 64, or 256 subregions, for each realization (as denoted by S859-X in Table 2), and then perform the jackknife covariance estimation for each case. The circle symbols show the average of the 480 covariance matrices. For comparison, we also show the full covariance matrix. The lower panel shows the ratio of each jackknife covariance relative to the full covariance. The jackknife curve traces the full covariance within the corresponding separation of the projected size of jackknife subregion for the mean lens redshift ($\bar{z}_1 \simeq 0.18$), and then starts to decrease at the larger separations as shown by the dashed curve. *Right:* Similarly to the left panels, but for the subsample covariance method. Here we plot the result up to the scale corresponding to the projected size of subregion for the mean lens redshift.

4.1.2 Effect of shape noises

We then examine the impact of shape noises on the comparison between the JK and full covariance methods. We use the 480 realizations as denoted by S859-jk2 in Table 2. We add, to the simulated shear at each pixel in the source plane ($z_s = 1$), a random ellipticity assuming the Gaussian distribution given by

$$P(e) = \frac{1}{\pi\sigma_{\text{int}}^2} \exp\left(-\frac{e^2}{\sigma_{\text{int}}^2}\right), \quad (27)$$

where $e^2 = e_1^2 + e_2^2$ and $\sigma_{\text{int}}^2 = \sigma_e^2 / (n_{\text{gal}} \theta_{\text{pix}}^2)$ with the pixel size of 0.43 arcmin. We then assume a random orientation to determine the two ellipticity components. Here, we set $\sigma_e = 0.35$ and study two cases of $n_{\text{gal}} = 1$ or 20 arcmin^{-2} . The former source number density corresponds to a typical value of the imaging survey in SDSS, while the latter is for imaging surveys such as the Subaru Hyper Suprime-Cam survey.

Fig. 5 compares the JK and full variances in the presence of shape noises. In the case of $n_{\text{gal}} = 1 \text{ arcmin}^{-2}$ where the shape noise gives a greater contribution to the variance over the wider range of R , the JK method gives a reasonably good agreement with the full variance up to the projected size of JK subregion at the mean lens redshift. In the case of $n_{\text{gal}} = 20 \text{ arcmin}^{-2}$ where the sample variance gives a greater contribution relative to the shape noise, the JK variance gives a good agreement with the full variance in the shape noise dominated regime, $R \lesssim 10 \text{ Mpc}/h$ for this case, but shows about 10% underestimation in the error (20% in the variance) at the radius corresponding to the JK subregion size (denoted by the arrow in the x -axis). The underestimation becomes greater at radii beyond the JK subregion size.

4.1.3 Area dependence of SSC in the full covariance

Is the variance of galaxy-galaxy weak lensing is sensitive to the SSC term? Fig. 6 addresses this question, showing how the diagonal components of the full covariance scale with the survey area. Here we consider the light-cone simulations for different areas of $f_{\text{sky}} = 1/12, 1/48, 1/192$ and $1/768$ corresponding to $\Omega_s \simeq 3437, 859, 215$ and 54 sq. degrees, respectively, for the mass-limited sample of lensing halos with $M_{200\text{m}} \geq 10^{13.5} h^{-1} M_{\odot}$ as used in Figs. 3 and 4. These simulations are given by ‘‘SXXX-full’’ in Table 2. The survey footprints for these simulations are defined by the HEALPIX pixelization. The footprint of each realization for the largest area, $f_{\text{sky}} = 1/12$, is given by one HEALPIX pixel, set by the parameter $n_{\text{side}} = 1$. Then the smaller area realizations are defined by further, hierarchical HEALPIX pixelizations of each region of $f_{\text{sky}} = 1/12$. By doing in this way, we use exactly the same light-cone simulations for this comparison study. Hence the difference in the covariance should arise from the SSC term, i.e. the effect of super-survey modes for each survey footprint.

Fig. 6 shows the diagonal component of the full covariance, multiplied by $(4\pi f_{\text{sky}})^{1/2}$. If the covariance scales with $1/f_{\text{sky}}$, all the curves should coincide, which is indeed the case at small separations, $R \lesssim 10 h^{-1} \text{ Mpc}$. In this regime, the error bars scale with the number

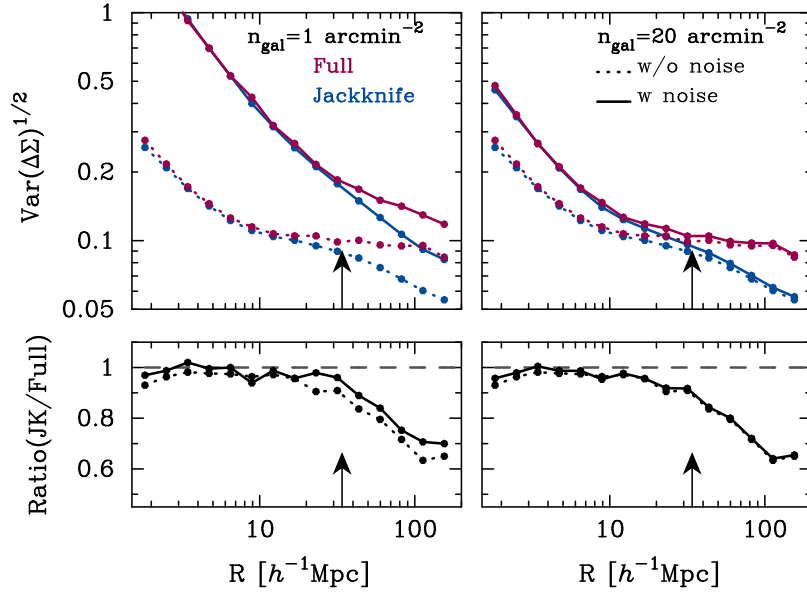


Figure 5. The effect of shape noises in the covariance estimations. In this figure, we used the same 480 realizations as in Fig. 3 with 64 subdivisions for each realization. When performing the covariance estimation, we include the shape noise contribution by adding the Gaussian noise with a fixed rms of shape ellipticities of 0.35, but different number density of sources is assumed. The arrow in each panel corresponds to the projected size of JK subregion for the mean lens redshift ($\bar{z}_1 \simeq 0.18$). *Left panels:* The case of source number density of 1 arcmin^{-2} , corresponding to the current survey such as the SDSS. The blue and red lines show the JK and the full variance, respectively. For each covariance, the solid line represents the presence of shape noises, while the dashed line is for the absence of shape noises. The lower panel shows the ratio of each JK covariance relative to the full covariance. *Right:* Similarly to the left panels, but for the case of source number density of 20 arcmin^{-2} .

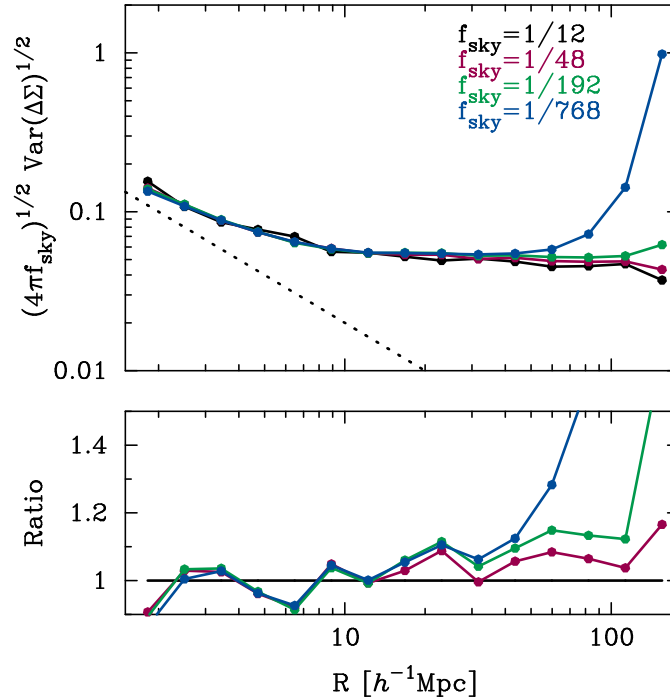


Figure 6. The dependence of the full covariance on the sky coverage, $f_{\text{sky}} = 1/12, 1/48, 1/192$ or $1/768$, respectively. We used exactly the same realizations of different numerical measurements. We plot the covariance matrix for each case, multiplied by a factor of $(4\pi f_{\text{sky}})^{1/2}$, such that all the covariance matrices agree with each other if the covariance matrix scales with the sky fraction as $\mathbf{C} \propto 1/f_{\text{sky}}$. If the covariance scales with the inverse of the number of source-lens pairs, it should scale with R as $\mathbf{C} \propto 1/N_{\text{pair}} \propto [R^2 \Delta \ln R]^{-1}$ for the logarithmically spaced bins, as denoted by the dotted line. In the bottom panel, we show the ratio of the different covariance matrices relative to the covariance for the largest area case ($f_{\text{sky}} = 1/12$), which has a minimum impact of the SSC term (see text for details).

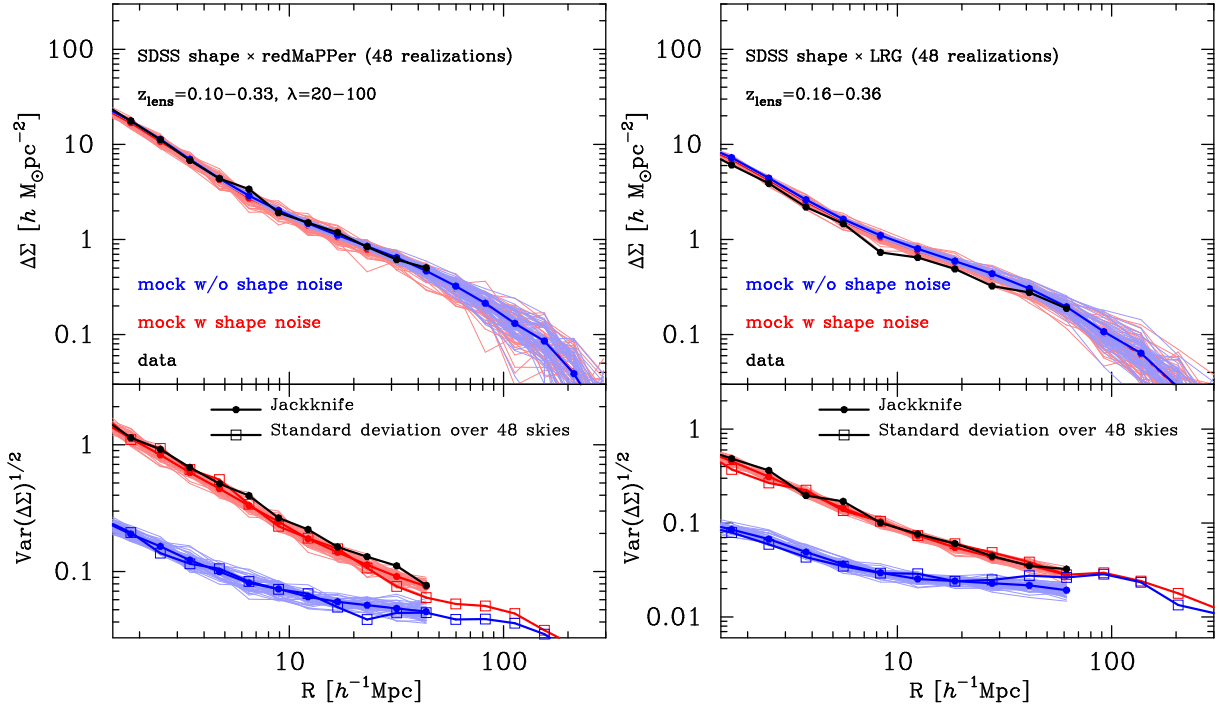


Figure 7. Comparison of the stacked signals measured from the mock catalogs and the real SDSS data, for the redMaPPer clusters (left panels) and LRGs (right), respectively. To do this, we used the 48 realizations of full-sky, light-cone simulations for the Λ CDM cosmology; we populate the real SDSS source galaxies (their sky distribution and intrinsic shapes), simulate the lensing effects on each source galaxy and identify hypothetical redMaPPer clusters or LRGs in the halo catalogs (see Section 3). We also properly take into account the footprints for both the source galaxies and the lensing objects in Fig. 2. In each panel, the upper plot shows the stacked lensing profiles, where we employ the same logarithmically-spacing binning as used in Miyatake et al. (2016b). The black circle symbols are the measurements from the SDSS data; we used the results of Miyatake et al. (2016b) for the redMaPPer clusters and re-performed the LRG weak lensing measurements for $\Delta\Sigma(R)$ following Mandelbaum et al. (2013) (see text for details), respectively. The red points are the average of the 48 realizations, while the thin curve shows the result for each realization. For comparison, the blue point and the thin curve show the results without shape noise. The lower plot shows the diagonal components of the covariance matrix for the full covariance method or the jackknife method, where we used the same jackknife subdivision in Fig. 2 as in the measurements. The black points are the jackknife covariance estimated from the real SDSS data. Our light-cone simulations fairly well reproduce the signals and JK covariances from the real SDSS data.

of pairs between source and lensing halos, leading to $[\text{Var}(\Delta\Sigma)]^{1/2} \propto [1/R^2 \Delta \ln R]^{1/2} \propto 1/R$ for the fixed logarithmic binning of R , as denoted by the dotted line. At the larger separations, the scaling of covariance with $1/f_{\text{sky}}$ breaks down. The full covariance with smaller total area starts to deviate from the covariance of $f_{\text{sky}} = 1/12$ at a smaller separation, because it has a greater contribution of the SSC term. Together with the results in Fig. 4, one might think that, by measuring the JK covariances as a function of different subdivisions, we can infer the full covariance for the total area of a given survey by scaling the JK covariance according to the area dependence of the SSC term shown in Fig. 6. However, this would be difficult in practice because the JK covariance estimation can be noisy for a particular one realization (see below), especially when the dimension of data vector is large, and also because the SSC term depends on the geometry of survey footprints, and therefore cannot be specified by the single quantity f_{sky} even if the underlying cosmological model is known (Takada & Hu 2013; Takahashi et al. 2014). From the results in Figs. 3–6, we conclude that the SSC term is a subdominant source of the sample variance at $R \lesssim 30 h^{-1} \text{Mpc}$, corresponding to the typical largest scale in the current stacked lensing analyses, while the SSC term can be significant at $R \sim 100 h^{-1} \text{Mpc}$. In Appendix B, we show off-diagonal terms of the full covariance matrix as in Figure 6.

4.2 Application to SDSS data: redMaPPer clusters and LRGs

Now we move to an application of our method to the real SDSS data, the catalogs of redMaPPer clusters and LRGs. We again emphasize that we utilize 48 realizations of full-sky simulations as described in Section 3: we populate the real catalog of SDSS source galaxies into the source planes, define the survey footprints, identify hypothetical lensing objects in each lens plane and simulate the lensing effect on each source galaxy. For each mock catalog, we measured the stacked lensing profiles. We then implemented the covariance estimations: we combined all the 48 realizations to estimate the full covariance, while we performed the JK covariance estimation for each realization. Note that, for this study, we used the JK resampling method to remove only the lensing objects in each subregion, but use all the source galaxies for each JK resample, as used in the measurements.

The left panels of Fig. 7 show the result for our mock realizations of the redMaPPer clusters. We used the same logarithmically-spacing binning of radial separations as used in Miyatake et al. (2016b). The upper plot shows that our mock catalogs well reproduce the stacked

lensing profile measured from the real SDSS data over the range of radii we considered. The lower plot compares the diagonal components of covariance matrix at each radial bin, measured from the mock catalog and also from the real data. The thin red curves show the covariance matrix at each radial bin, measured from each realization based on the JK method. The bold red circle shows the average of 48 JK covariance matrices, and can be compared with the JK covariance measured from the real SDSS data in [Miyatake et al. \(2016b\)](#). It can be found that our mock catalog fairly well reproduces the JK covariance of the real data. The square symbol shows the full covariance, which matches the JK errors at $R \lesssim 50 - 60 h^{-1} \text{ Mpc}$. These results show that the JK estimator gives an unbiased estimator of the covariances when the separation scale is smaller than the size of JK region. We again note that the agreement is realized, if the random catalog subtraction is implemented as claimed in [Singh et al. \(2016\)](#). When the random subtraction is not implemented, we find that the JK method over-estimates the errors at $R \gtrsim 10 - 20 h^{-1} \text{ Mpc}$. For comparison, the blue-thin curves and -circle symbols show the full or JK covariances without the shape noise contamination. Comparing the red and blue curves manifests that the covariances at $R \gtrsim 50 h^{-1} \text{ Mpc}$ are in the sample variance regime for the SDSS number density of source galaxies ($\bar{n}_{\text{gal}} \sim 1 \text{ arcmin}^{-2}$). For the full covariance case, we can use the stacked lensing measurements up to the greater separations than in the JK method, where we can use the measurements only up to the maximum separation corresponding to the size of JK subregion.

The right panel of Fig. 7 shows the similar results for the SDSS LRGs. Note that [Mandelbaum et al. \(2013\)](#) used the compensated weak lensing profile $\Upsilon(R; R_0)$, which is designed to remove the small-scale information at $R \lesssim 4 \text{ Mpc}/h$, for the cosmological analysis. They carefully discussed the covariance matrix for the Υ -profile, and found that it appears to be less sensitive to the non-Gaussian sample variance due to the nature of the statistic. In this paper, we re-performed the measurements of $\Delta\Sigma(R)$ for the same LRG sample, and estimated the JK covariance following the JK subdivision in [Mandelbaum et al. \(2013\)](#). The agreements between the JK covariances from our mock catalogs and the real data are somewhat better, probably due to the higher number density of LRGs than that of the redMaPPer clusters.

In Appendix C we study the off-diagonal components of the covariance matrix, and found that the JK covariance, estimated from one particular realization, can be noisy and cannot reliably estimate the off-diagonal components, if an insufficient number of JK subregions are used.

4.3 Implications for cosmological analysis

4.3.1 An improvement in the signal-to-noise ratio due to the use of accurate covariance

As we have so far shown, the JK covariance is noisy on each realization basis, although it gives a reasonably accurate estimation of the true covariance on average. In addition, the JK covariance is valid only up to the size of JK subregion. Therefore the use of an accurate covariance in cosmological analysis should become important to obtain robust results. (1) The JK covariance can be noisy, because the covariance is estimated from a particular realization, i.e. the real data, and if the number of the JK subregions is not sufficient. (2) Since the JK method sets a maximum separation scale corresponding to the size of JK subregion in the cosmological analysis, the use of the full covariance, estimated from the mock catalogs, gives us an access to the larger separations, where there is a cleaner cosmological information in the weakly nonlinear or linear regime. (3) The JK method tends to under-estimate the true covariance at the boundary of JK subregion for a survey with higher number density of source galaxies.

In order to quantify the information content obtained from the use of the accurate covariance, we study the cumulative signal-to-noise ratios for measuring the stacked lensing in the sample variance limited regime:

$$\left(\frac{S}{N}\right)^2 = \sum_{R_{\min} < \{R_i, R_j\} < R_{\max}} \widehat{\Delta\Sigma}(R_i) \mathbf{C}_{ij}^{-1} \widehat{\Delta\Sigma}(R_j), \quad (28)$$

where $\widehat{\Delta\Sigma}(R_i)$ denotes the stacked lensing signal for the i -th radius R_i , \mathbf{C} is the covariance matrix, and \mathbf{C}^{-1} is its inverse. When inverting the matrix, we use the singular value decomposition for the matrix of \mathbf{C} in the range of R defined by equation (28). Note that, when estimating the inverse matrix \mathbf{C}^{-1} , we included the correction factor of $N_r/[N_r - N_d - 1]$ proposed in [Hartlap, Simon & Schneider \(2007\)](#), where N_r is the number of the realizations and N_d is the dimension of data. The summation runs over all the radial bins in the range of $R_{\min} < R < R_{\max}$. Here we set $R_{\min} \simeq 8 h^{-1} \text{ Mpc}$ in order to focus on the scales in the weakly nonlinear or linear regime, the so-called two-halo term, where a cleaner cosmological information can be extracted. The cumulative signal-to-noise ratio includes the contribution of off-diagonal covariance components and is independent of the radial bin width, while the covariance matrix itself depends on the width (the Gaussian covariance term depends on the bin width, since the number of lens-source pairs in a given bin depends on the width).

Fig. 8 shows the cumulative signal-to-noise ratio, S/N , for the redMaPPer clusters and LRGs samples as a function of the maximum separation R_{\max} . To compute these, we use the signals of the real SDSS data up to the JK maximum scale, and then use the signal measured from the mock catalog at the greater separations. As for the covariance matrix, we use the different covariance matrices in Fig. 7, which are estimated from the real data itself based on the JK method or from the 48 realizations of the mock catalogs based on the full covariance or JK method. The thin red curves show the S/N values for each of 48 realizations, while the black curve in each panel is the value obtained from the SDSS data ([Miyatake et al. 2016b](#)). Note that the red and black curves are shown up to $R_{\max} \sim 50 - 70 h^{-1} \text{ Mpc}$ corresponding to the size of JK subregion. The figure shows that the S/N value for the real data is on a relatively lower side of the 48 realizations, perhaps due to the statistical variance. The bottom panel of each plot shows the signal-to-noise ratio per each bin, displaying $S/N \geq 1$ for the lensing signals up to the separation $R \simeq 100 h^{-1} \text{ Mpc}$, beyond a size of the JK subregion. Such large-scale lensing signals will be useful to extract

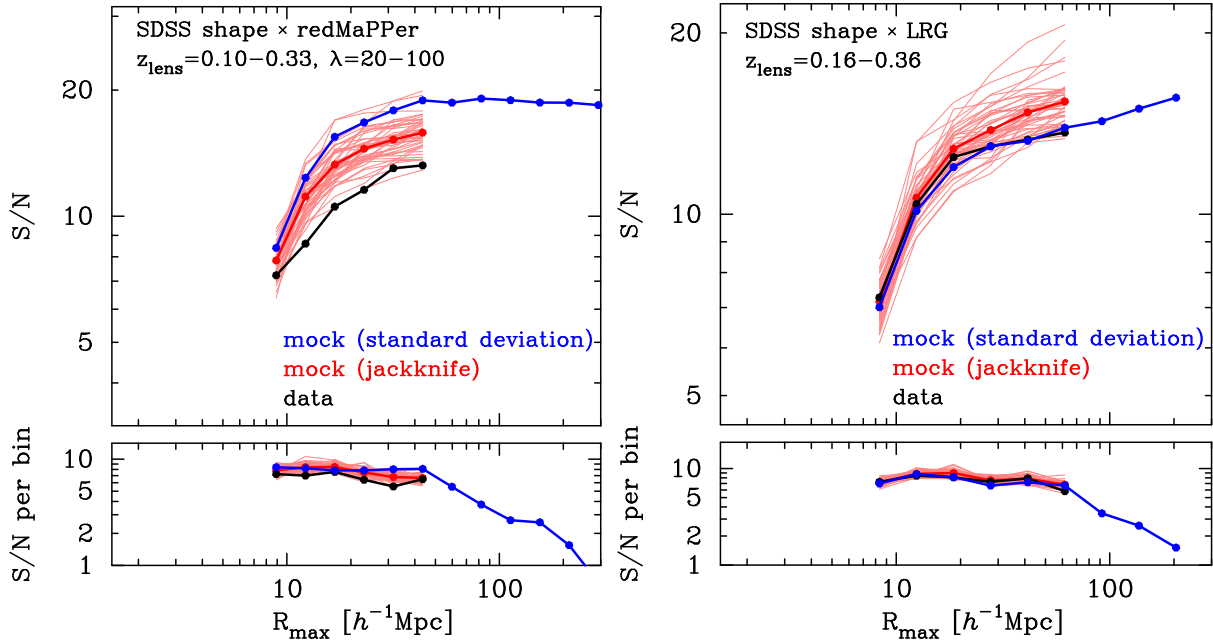


Figure 8. *Upper panels:* The cumulative signal-to-noise ratio S/N , integrated over $8[h^{-1} \text{Mpc}] \leq R \leq R_{\text{max}}$, as a function of R_{max} for the stacked lensing measurements for the redMaPPer cluster and LRG samples estimated from the real data and the mock catalogs. The stacked lensing signals at $R \gtrsim 10 h^{-1} \text{Mpc}$ are in the two-halo term regime and expected to contain a cleaner cosmological information. To compute the curve for the full covariance case, we used the actual signals measured from the real data up to $R \simeq 50 h^{-1} \text{Mpc}$, and then used the simulated signals at the larger separations. The lower panels show the S/N value at each separation bin. The use of the full covariance enables us to use larger separation beyond the size of JK subregion, where there are signals with $S/N \gtrsim 1$ still available in each bin.

useful cosmological information on the baryonic acoustic oscillations, the parameters of primordial power spectrum (e.g., Jeong, Komatsu & Jain 2009), the primordial non-Gaussianity (Dalal et al. 2008), and neutrino masses (e.g., Takada, Komatsu & Futamase 2006; Saito, Takada & Taruya 2009; LoVerde 2014).

5 CONCLUSION AND DISCUSSION

In this paper, we have developed a method to create a mock catalog of the cross-correlation between positions of lensing objects and shapes of background galaxies – the stacked lensing of galaxy clusters or galaxy-galaxy weak lensing. To do this, we fully utilized the full-sky, light-cone simulations based on a suit of multiple N -body simulation outputs, where the lensing fields of source galaxies are given in multiple shells in the radial direction out to a maximum source redshift $z_s \simeq 2.4$ as well as the halo catalogs in lens planes are given in the light cone. Our method enables one to generate a mock catalog of the stacked lensing following the procedures; (1) define the survey footprints based on the assigned RA and dec coordinates in the full-sky simulation, (2) populate the real catalog of source galaxies into the light-cone simulation realization according to the angular position (RA and dec) and redshift of each source galaxy, (3) randomly rotate the ellipticity of each source galaxy to erase the real lensing effect, (4) simulate the lensing effects on each source galaxy, using the lensing fields in the light-cone simulation, and (5) identify halos that are considered to host galaxies or clusters of interest, according to a prescription to connect the galaxies or clusters to halos (e.g. the scaling relation between halo mass and cluster richness or the halo occupation distribution model for galaxies). With this method, we can use the observed properties of data, the survey footprints and the positions and characteristics of source galaxies (the intrinsic ellipticities and the redshift distribution). We applied this method to the real SDSS catalog of source galaxies as well as the SDSS catalogs of redMaPPer clusters or luminous red galaxies (LRGs), as shown in Fig. 2. We then showed that our mock catalogs well reproduce the signals as well as the jackknife (JK) covariance error bars, estimated from the real data (Fig. 7). Our method will be powerful to estimate the error covariance matrix for ongoing and upcoming wide-field weak lensing surveys.

By having the accurate mock catalogs of cluster/galaxy-shear cross correlation, we were able to study the nature of the error covariance matrix. In particular we focused on addressing validity and limitation of the JK method, which has been often used in the literature. The JK method is based on the real data itself, therefore referred to as an internal covariance estimator, and is known in the fields of statistics or data science to give an unbiased estimator of the covariance if the field is Gaussian or Poissonian. We found that the JK method gives a reasonably accurate estimation of the true covariance to within 10% in the amplitude on average, at separation scales smaller than the size of JK subregion, but it can under-estimate the true error at the larger separations, especially for a survey with higher number density of source galaxies as in ongoing and upcoming surveys such as the Subaru HSC survey. However we should keep in mind a limitation for the use of the JK method: the JK covariance can be noisy on each realization basis, because the JK covariance is estimated from a particular

realization (i.e. data). The JK covariance matrix becomes noisier or unreliable if the number of JK subregions/resamples is small or if the dimension of data vector is comparable with the number of JK subregions. Thus the use of accurate covariance matrix for the stacked lensing measurement is important in the future cosmological analysis. The full covariance gives us an access to larger separations beyond the scale of JK subregion, where the JK covariance ceases to be valid (Fig. 4). We showed that the full covariance gives signals with $S/N \geq 1$ out to about $100 h^{-1}$ Mpc in the projected separation. Thus the use of accurate covariance for the stacked lensing is highly desirable in order to attain the full potential of ongoing and upcoming surveys. In particular such large-scale weak lensing signals are expected to contain useful information on the fundamental physics such as the baryon acoustic oscillations, the primordial power spectrum, the primordial non-Gaussianity and the neutrino mass. Exploring an improvement in the cosmological parameters from the SDSS data by the use of the accurate covariance is our future work and will be presented elsewhere.

Combining the stacked lensing and auto-correlation measurements for the same foreground tracers allows one to improve cosmological constraints by recovering the underlying dark matter clustering against the bias uncertainty (Seljak et al. 2005; Mandelbaum et al. 2013; More et al. 2015). This would also be true even if the foreground objects are affected by the assembly bias uncertainty if the two measurements are properly combined (Miyatake et al. 2016b; McEwen & Weinberg 2016). Furthermore it would be interesting to combine the stacked lensing with the redshift-space distortion (RSD) measurement for the same foreground galaxies in order to improve cosmological constraints as well as test gravity theory on cosmological scales, by calibrating small-scale systematic effects in the RSD measurement such as the Finger-of-God effect (Hikage, Takada & Spergel 2012; Hikage et al. 2013). A joint experiment of galaxy weak lensing and CMB weak lensing for the same foreground clusters/galaxies can be used to directly measure the lensing efficiency function, $\Sigma_{\text{cr}}(z_l, z_s)$, without being affected by nonlinear structure formation including unknown baryonic physics as well as to calibrate multiplicative systematic biases in the CMB lensing or galaxy weak lensing that is otherwise difficult to calibrate with either method alone (Das & Spergel 2009; Schaan et al. 2016; Miyatake et al. 2016a). Thus once one starts to combine different clustering measurements, the dimension of data vector quickly increases and the calibration of auto- and cross-covariances is more demanding. For this reason, it would be desirable to develop a hybrid method of combining the mock light-cone catalog of large-scale structures containing various fields (weak lensing, halos and velocity fields) and the analytical method to model the SSC terms in different observables. This seems feasible, and will be our future work.

ACKNOWLEDGMENTS

We thank Rachel Mandelbaum for making the SDSS galaxy catalogs and the jackknife subdivisions available to us as well as for useful discussion. We thank Nick Battaglia, Bhuvnesh Jain, Surhud More, Uros Seljak and Matias Zaldarriaga for useful discussion. M.S. is supported by Research Fellowships of the Japan Society for the Promotion of Science (JSPS) for Young Scientists. H.M. is supported by the Jet Propulsion Laboratory, California Institute of Technology, under a contract with the National Aeronautics and Space Administration. Ry.M. is supported by Advanced Leading Graduate Course for Photon Science. This work was in part supported by Grant-in-Aid for Scientific Research from the JSPS Promotion of Science (JP23340061 and JP26610058), MEXT Grant-in-Aid for Scientific Research on Innovative Areas (15H05887, JP15H05893, JP15K21733, JP15H05892) and by JSPS Program for Advancing Strategic International Networks to Accelerate the Circulation of Talented Researchers. Numerical computations presented in this paper were in part carried out on the general-purpose PC farm at Center for Computational Astrophysics, CfCA, of National Astronomical Observatory of Japan.

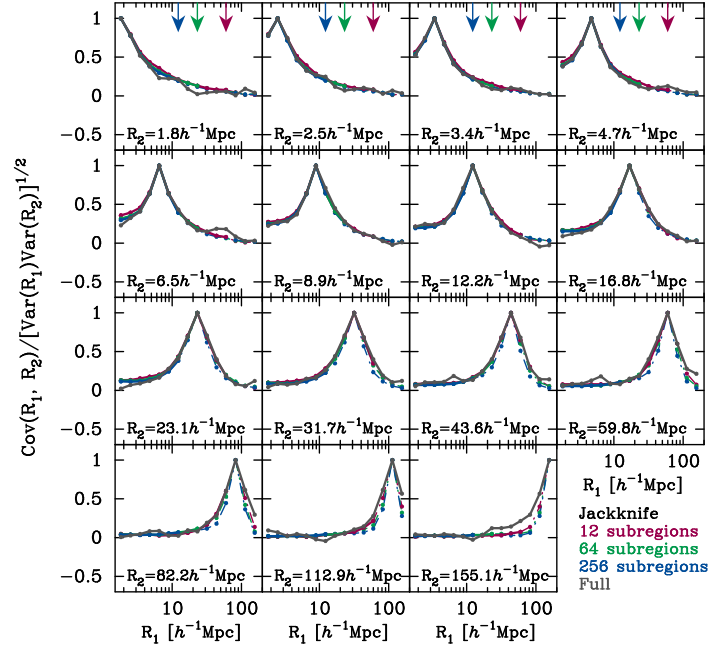


Figure A1. The off-diagonal components of the jackknife covariance normalized the diagonal components, $r_{ij} = C(R_i, R_j) / \sqrt{C(R_i, R_i)C(R_j, R_j)}$, estimated from the mock realizations of galaxy-galaxy weak lensing measurements. We use the same realizations as in Figure 4. The different panels show the cross-correlation coefficients for different separation R_i as indicated by the legend. In the top panels, the colored arrows show the corresponding R to the size of each JK subregion.

APPENDIX A: DEPENDENCE OF NUMBER OF SUBREGIONS ON OFF-DIAGONAL COMPONENTS OF THE JACKKNIFE COVARIANCE MATRIX

In this appendix, we show the off-diagonal components of JK covariance matrices measured from the mock simulations of galaxy-galaxy lensing. We assume a hypothetical survey with the sky fraction of $f_{\text{sky}} = 1/48$ and the source redshift of $z_s = 0.5$. As lens objects, we consider a sample of mass-selected halos with $M_{200\text{m}} \geq 10^{13.5} h^{-1} M_{\odot}$ and in the redshift range $z_1 = [0.1, 0.27]$. In order to compute the covariance, we use the realizations as dubbed “S859-full”, “S859-jk1”, “S859-jk2” and “S859-jk3” in Table 2. Fig. A1 shows the off-diagonal components of JK covariance when we vary the size of JK subregion. We found that the impact of the number of JK regions on the covariance estimation is more prominent for the diagonal part. Once the off-diagonal components are normalized by the diagonal components, the effect of number of subregions is found to be $\sim 20\%$ at largest.

APPENDIX B: AREA DEPENDENCE IN OFF-DIAGONAL COMPONENTS OF THE FULL COVARIANCE MATRIX

In this appendix, we examine the area dependence in the off-diagonal components of full covariance matrices as in Section 4.1.3. Here we use the realizations of “SXXX-full” in Table 2. The results are summarized in Fig. B1. The area dependence in the off-diagonal components is found to be relatively small compared to the diagonal one.

APPENDIX C: OFF-DIAGONAL COMPONENTS OF THE SDSS COVARIANCE MATRIX

In this appendix, we show the off-diagonal components of JK covariance matrices measured from 48 mock simulations of galaxy-galaxy lensing. Figs. C1 and C2 show the off-diagonal components for the redMaPPer clusters and LRGs, respectively, comparing the results from the actual data and the mock catalogs. The figures show that the JK covariance obtained from one particular realization can be noisy, and is biased from the underlying true covariance. Here the average matrix of the 48 JK covariances is considered to be close to the full covariance for the JK subregion (see main text for details).

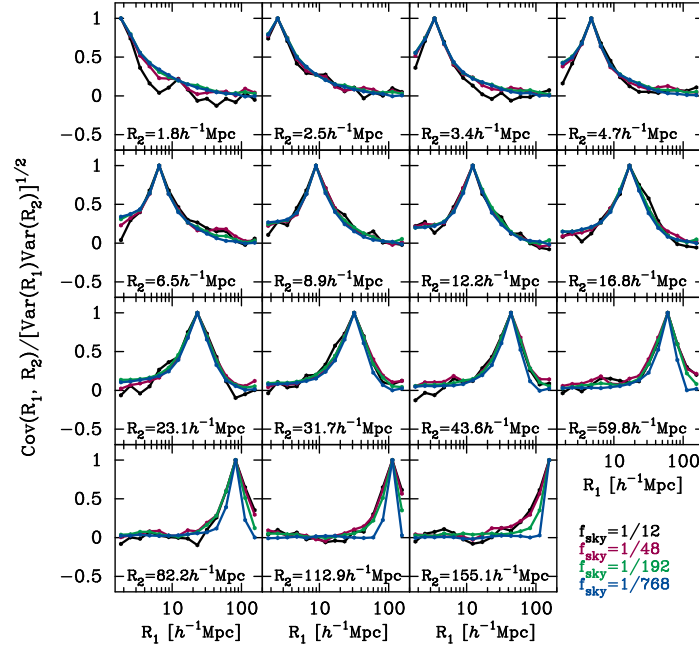


Figure B1. The off-diagonal components of the jackknife covariance normalized the diagonal components, $r_{ij} = C(R_i, R_j) / \sqrt{C(R_i, R_i)C(R_j, R_j)}$, estimated from the mock realizations of galaxy-galaxy weak lensing measurements. We use the same realizations as in Figure 6.

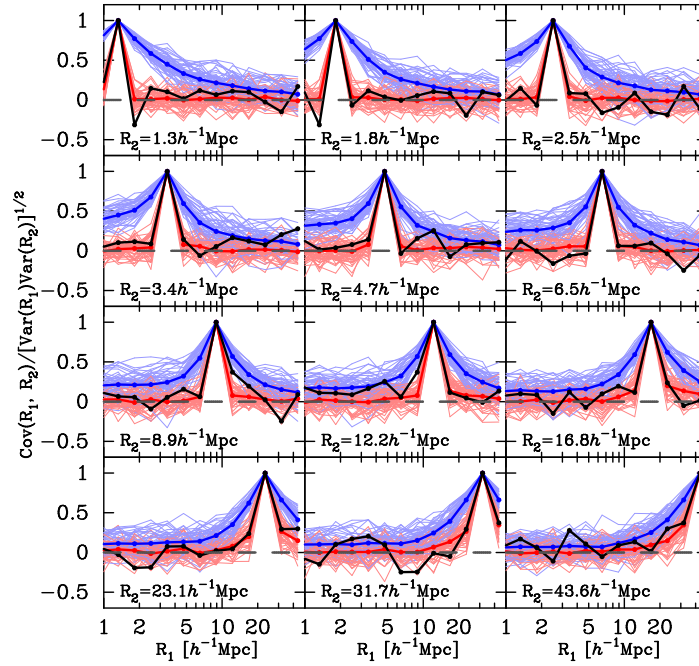


Figure C1. The off-diagonal components of the jackknife covariance normalized the diagonal components, $r_{ij} = C(R_i, R_j) / \sqrt{C(R_i, R_i)C(R_j, R_j)}$, estimated from the real data and mock catalogs of the redMaPPer clusters. The different panels show the cross-correlation coefficients for different separation R_i as indicated by the legend. The black line shows the result from the real data, and the thin red line shows the result obtained from each of the 48 mock catalogs. The bold red line is the average of the 48 results. The blue lines are the results for the mock catalogs without shape noise.

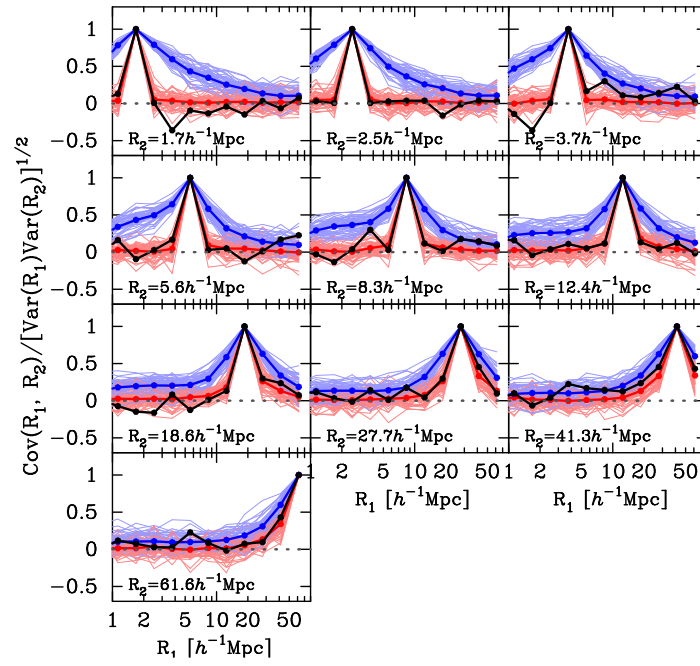


Figure C2. Similar to Fig. C1, but for the luminous red galaxies.

REFERENCES

- Aihara H. et al., 2011, *ApJS*, 193, 29
 Becker M. R. et al., 2015, *ArXiv e-prints*
 Behroozi P. S., Wechsler R. H., Wu H.-Y., 2013, *ApJ*, 762, 109
 Beltrán Jiménez J., Durrer R., 2011, *Phys. Rev. D*, 83, 103509
 Bernstein G. M., Jarvis M., 2002, *AJ*, 123, 583
 Bothun G. D., Geller M. J., Beers T. C., Huchra J. P., 1983, *ApJ*, 268, 47
 Brainerd T. G., Blandford R. D., Smail I., 1996, *ApJ*, 466, 623
 Cacciato M., van den Bosch F. C., More S., Li R., Mo H. J., Yang X., 2009, *MNRAS*, 394, 929
 Cacciato M., van Uitert E., Hoekstra H., 2014, *MNRAS*, 437, 377
 Clampitt J. et al., 2016, *ArXiv e-prints*
 Cooray A., Hu W., 2001, *ApJ*, 554, 56
 Coupon J. et al., 2015, *MNRAS*, 449, 1352
 Crocce M., Pueblas S., Scoccimarro R., 2006, *MNRAS*, 373, 369
 Dalal N., Doré O., Huterer D., Shirokov A., 2008, *Phys. Rev. D*, 77, 123514
 Das S., Spergel D. N., 2009, *Phys. Rev. D*, 79, 043509
 Dodelson S., Schneider M. D., 2013, *Phys. Rev. D*, 88, 063537
 Efron B., 1982, *The Jackknife, the Bootstrap and other resampling plans*
 Eisenstein D. J. et al., 2001, *AJ*, 122, 2267
 Fischer P. et al., 2000, *AJ*, 120, 1198
 Gillis B. R. et al., 2013, *MNRAS*, 431, 1439
 Górski K. M., Hivon E., Banday A. J., Wandelt B. D., Hansen F. K., Reinecke M., Bartelmann M., 2005, *ApJ*, 622, 759
 Guzik J., Seljak U., 2002, *MNRAS*, 335, 311
 Hamana T., Mellier Y., 2001, *MNRAS*, 176, 169
 Hamilton A. J. S., Rimes C. D., Scoccimarro R., 2006, *MNRAS*, 371, 1188
 Harnois-Déraps J. et al., 2016, *MNRAS*
 Hartlap J., Simon P., Schneider P., 2007, *A&A*, 464, 399
 Hikage C., Mandelbaum R., Takada M., Spergel D. N., 2013, *MNRAS*, 435, 2345
 Hikage C., Takada M., Spergel D. N., 2012, *MNRAS*, 419, 3457
 Hildebrandt H. et al., 2016, *ArXiv e-prints*
 Hinshaw G. et al., 2013, *ApJS*, 208, 19
 Hirata C., Seljak U., 2003, *MNRAS*, 343, 459
 Hoekstra H., Yee H. K. C., Gladders M. D., 2004, *ApJ*, 606, 67
 Hu W., Kravtsov A. V., 2003, *ApJ*, 584, 702
 Hudson M. J., Gwyn S. D. J., Dahle H., Kaiser N., 1998, *ApJ*, 503, 531
 Jeong D., Komatsu E., Jain B., 2009, *Phys. Rev. D*, 80, 123527
 Johnston D. E. et al., 2007, *ArXiv e-prints*
 Kayo I., Takada M., 2013, *ArXiv e-prints*
 Kayo I., Takada M., Jain B., 2013, *MNRAS*, 429, 344
 Kazin E. A. et al., 2010, *ApJ*, 710, 1444
 Krause E., Eifler T., 2016, *ArXiv e-prints*
 Kwan J. et al., 2016, *ArXiv e-prints*
 Landy S. D., Szalay A. S., 1993, *ApJ*, 412, 64
 Lewis A., Challinor A., Lasenby A., 2000, *ApJ*, 538, 473
 Li Y., Hu W., Takada M., 2014a, *Phys. Rev. D*, 89, 083519
 Li Y., Hu W., Takada M., 2014b, *Phys. Rev. D*, 90, 103530
 Lima M., Hu W., 2005, *Phys. Rev. D*, 72, 043006
 LoVerde M., 2014, *Phys. Rev. D*, 90, 083530
 Mandelbaum R. et al., 2005, *MNRAS*, 361, 1287
 Mandelbaum R., Seljak U., Kauffmann G., Hirata C. M., Brinkmann J., 2006, *MNRAS*, 368, 715
 Mandelbaum R., Slosar A., Baldauf T., Seljak U., Hirata C. M., Nakajima R., Reyes R., Smith R. E., 2013, *MNRAS*, 432, 1544
 McEwen J. E., Weinberg D. H., 2016, *ArXiv e-prints*
 Miralda-Escude J., 1991, *ApJ*, 380, 1
 Miyatake H., Madhavacheril M. S., Sehgal N., Slosar A., Spergel D. N., Sherwin B., van Engelen A., 2016a, *ArXiv e-prints*
 Miyatake H., More S., Takada M., Spergel D. N., Mandelbaum R., Rykoff E. S., Rozo E., 2016b, *Phys. Rev. Lett.*, 116, 041301
 Mohammed I., Seljak U., Vlah Z., 2016, *ArXiv e-prints*
 More S., Miyatake H., Mandelbaum R., Takada M., Spergel D. N., Brownstein J. R., Schneider D. P., 2015, *ApJ*, 806, 2
 Nakajima R., Mandelbaum R., Seljak U., Cohn J. D., Reyes R., Cool R., 2012, *MNRAS*, 420, 3240
 Navarro J. F., Frenk C. S., White S. D. M., 1997, *ApJ*, 490, 493
 Nishimichi T. et al., 2009, *Publications of the Astronomical Society of Japan*, 61, 321
 Norberg P., Baugh C. M., Gaztañaga E., Croton D. J., 2009, *MNRAS*, 396, 19
 Oguri M., Takada M., 2011, *Phys. Rev. D*, 83, 023008
 Okabe N., Smith G. P., Umetsu K., Takada M., Futamase T., 2013, *ApJ*, 769, L35
 Reid B. A., Spergel D. N., 2009, *ApJ*, 698, 143
 Reyes R., Mandelbaum R., Gunn J. E., Nakajima R., Seljak U., Hirata C. M., 2012, *MNRAS*, 425, 2610
 Rozo E., Rykoff E. S., 2014, *ApJ*, 783, 80
 Rozo E., Rykoff E. S., Bartlett J. G., Melin J.-B., 2015a, *MNRAS*, 450, 592

- Rozo E., Rykoff E. S., Becker M., Reddick R. M., Wechsler R. H., 2015b, *MNRAS*, 453, 38
- Rykoff E. S. et al., 2014, *ApJ*, 785, 104
- Saito S., Takada M., Taruya A., 2009, *Phys. Rev. D*, 80, 083528
- Sato M., Hamana T., Takahashi R., Takada M., Yoshida N., Matsubara T., Sugiyama N., 2009, *ApJ*, 701, 945
- Sato M., Takada M., Hamana T., Matsubara T., 2011, *ApJ*, 734, 76
- Schaan E., Krause E., Eifler T., Doré O., Miyatake H., Rhodes J., Spergel D. N., 2016, *ArXiv e-prints*
- Schaan E., Takada M., Spergel D. N., 2014, *Phys. Rev. D*, 90, 123523
- Scoccimarro R., Zaldarriaga M., Hui L., 1999, *ApJ*, 527, 1
- Seljak U. et al., 2005, *Phys. Rev. D*, 71, 043511
- Shirasaki M., Hamana T., Yoshida N., 2015, *MNRAS*, 453, 3043
- Shirasaki M., Yoshida N., 2014, *ApJ*, 786, 43
- Simet M., McClintock T., Mandelbaum R., Rozo E., Rykoff E., Sheldon E., Wechsler R. H., 2016, *ArXiv e-prints*
- Singh S., Mandelbaum R., Seljak U., Slosar A., Vazquez Gonzalez J., 2016, *ArXiv e-prints*
- Springel V., 2005, *MNRAS*, 364, 1105
- Takada M., Bridle S., 2007, *New Journal of Physics*, 9, 446
- Takada M. et al., 2014, *PASJ*, 66, R1
- Takada M., Hu W., 2013, *Phys. Rev. D*, 87, 123504
- Takada M., Jain B., 2009, *MNRAS*, 395, 2065
- Takada M., Komatsu E., Futamase T., 2006, *Phys. Rev. D*, 73, 083520
- Takada M., Spergel D. N., 2014, *MNRAS*, 441, 2456
- Takahashi R., Soma S., Takada M., Kayo I., 2014, *MNRAS*, 444, 3473
- Takahashi R. et al., 2009, *ApJ*, 700, 479
- Taylor A., Joachimi B., Kitching T., 2013, *MNRAS*, 432, 1928
- Tinker J., Kravtsov A. V., Klypin A., Abazajian K., Warren M., Yepes G., Gottlöber S., Holz D. E., 2008, *ApJ*, 688, 709
- Tinker J. L., Robertson B. E., Kravtsov A. V., Klypin A., Warren M. S., Yepes G., Gottlöber S., 2010, *ApJ*, 724, 878
- Valageas P., Nishimichi T., 2011, *Astronomy and Astrophysics*, 527, A87
- Velander M. et al., 2014, *MNRAS*, 437, 2111
- Wake D. A. et al., 2006, *MNRAS*, 372, 537
- York D. G. et al., 2000, *AJ*, 120, 1579
- Zheng Z. et al., 2005, *ApJ*, 633, 791